The development of the North Pacific Jet Phase Diagram as an objective tool to monitor the state of the upper-tropospheric flow pattern

By

ANDREW C. WINTERS[1*], DANIEL KEYSER[1], and LANCE F. BOSART[1]

[1]Department of Atmospheric and Environmental Sciences
University at Albany – State University of New York
Albany, NY 12222

Submitted for publication in ________________
XX XXX 2018

[*] *Corresponding author address:* Andrew C. Winters, Dept. of Atmospheric and Environmental Sciences, University at Albany, SUNY, 1400 Washington Ave., Albany, NY 12222. E-mail: acwinters@albany.edu

Abstract

Prior work has identified the leading modes of North Pacific Jet (NPJ) variability that prevail on synoptic timescales. The first leading mode corresponds to a zonal extension or retraction of the climatological NPJ, while the second leading mode corresponds to a poleward or equatorward shift of the exit region of the climatological NPJ. These NPJ regimes can strongly influence the character of the downstream large-scale flow pattern over North America. Consequently, knowledge of the prevailing NPJ regime offers value to operational medium-range (6–10-day) forecasts over North America. However, this value is limited without complementary knowledge of the characteristic forecast skill associated with each NPJ regime.

This study details the development of a NPJ Phase Diagram, which is constructed from the two leading empirical orthogonal functions of 250-hPa zonal wind anomalies during September–May 1979–2014 in the CFSR. The projection of 250-hPa zonal wind anomalies at any one or multiple times onto the NPJ Phase Diagram provides an objective characterization of the state or evolution of the upper-tropospheric flow pattern over the North Pacific. An analysis of 30 years of GEFS Reforecasts in the context of the NPJ Phase Diagram demonstrates that forecasts verifying during jet retractions and equatorward shifts are associated with larger average errors than jet extensions and poleward shifts. Furthermore, an examination of the top-10% best and worst forecasts suggests that periods characterized by rapid NPJ regime transition or the development and maintenance of North Pacific blocking events exhibit reduced forecast skill.

1. Introduction

Anchored downstream of the Asian continent at middle latitudes, the North Pacific jet (NPJ) stream is a narrow, meandering current of strong upper-tropospheric wind speeds bounded by considerable horizontal and vertical shear. The position and intensity of the NPJ is modulated by a number of external factors, including tropical convection (e.g., Hoskins and Karoly 1981; Madden and Julian 1994; Harr and Dea 2009; Archambault et al. 2013, 2015; Torn and Hakim 2015; Grams and Archambault 2016), interactions between the NPJ and baroclinic eddies along the midlatitude storm track (e.g., Orlanski and Sheldon 1995; Chang et al. 2002; Hakim 2003; Torn and Hakim 2015), and the East Asian Winter Monsoon (e.g., Jhun and Lee 2004; Lee et al. 2010; Wang and Chen 2014; Handlos and Martin 2016). In combination, these factors contribute to NPJ configurations that vary substantially on both weather and climate timescales.

In an attempt to better constrain the variability of the NPJ, prior work has identified the leading modes of NPJ variability that prevail on weather and climate timescales during the winter (Dec–Feb). Schubert and Park (1991) provided one of the first investigations of subseasonal NPJ variability, and calculated the two leading empirical orthogonal functions[1] (EOFs) of 20–70-day filtered zonal wind at 200 hPa over the Pacific basin. Their first EOF describes variability in the intensity of the NPJ over the western North Pacific, while their second EOF describes a zonal extension or retraction of the climatological NPJ. In contrast, Eichelberger and Hartmann (2007) employed daily zonal wind data during January in their analysis and found that the first EOF of the vertical-average zonal-mean zonal wind over the North Pacific encompasses variability in the intensity, longitudinal extent, and latitudinal

[1] An EOF analysis is a statistical technique to extract patterns that explain the greatest fraction of the variance within a multi-dimensional dataset (Wilks 2011).

position of the NPJ. Consequently, the Eichelberger and Hartmann (2007) analysis suggests that NPJ variability is considerably more complex when analyzed on synoptic timescales.

Recent studies by Athanasiadis et al. (2010) and Jaffe et al. (2011) have provided greater physical clarity on the two leading modes of NPJ variability that prevail on synoptic timescales during the cold season (Nov–Mar). These studies applied traditional EOF analysis to unfiltered upper-tropospheric zonal wind data over the North Pacific and determined that the first mode of NPJ variability corresponds to longitudinal variability in the extent of the NPJ. Specifically, a positive EOF 1 pattern (+EOF 1) describes a zonal extension of the climatological NPJ, while a negative EOF 1 pattern (–EOF 1) describes a zonal retraction of the climatological NPJ. The second mode of NPJ variability corresponds to latitudinal variability in the vicinity of the climatological exit region of the NPJ. In this sense, a positive EOF 2 pattern (+EOF 2) describes a poleward shift of the exit region of the climatological NPJ, while a negative EOF 2 pattern (–EOF 2) describes an equatorward shift.

Knowledge of the four NPJ configurations identified by Athanasiadis et al. (2010) and Jaffe et al. (2011), hereafter referred to as NPJ regimes, subsequently permits an examination of the relationship between each NPJ regime and the downstream large-scale flow pattern over North America. To this aim, Griffin and Martin (2017) employed time-extended EOF analyses of 250-hPa zonal wind data from the NCEP-NCAR reanalysis dataset (Kalnay et al. 1996) to construct composite analyses of the large-scale flow evolution over the North Pacific and North America during the 10-day period preceding and following the development of each NPJ regime. Provided with a clear relationship between each NPJ regime and the large-scale flow pattern over North America, the Griffin and Martin (2017) analysis implies that knowledge of the prevailing NPJ regime may offer considerable value to operational medium-range (6–10-day) forecasts of temperature and precipitation over North America. However, this value is limited operationally without complementary knowledge of the relative forecast skill associated with the development or persistence of each NPJ regime.

The concept of regime-dependent forecast skill has been explored in the context of large-scale upper-tropospheric flow regimes over the North Atlantic basin (e.g., Ferranti et al. 2015) and in the context of large-scale atmospheric teleconnection patterns (e.g., Palmer 1988; Lin and Derome 1996; Sheng 2002; Ferranti et al. 2015). However, to the authors' knowledge, no study has comprehensively examined regime-dependent forecast skill over the North Pacific in the context of the prevailing NPJ regime. Consequently, a primary goal of the present study is to identify whether certain NPJ regimes exhibit reduced or enhanced forecast skill. In an effort to address this goal, the results from prior studies on NPJ variability (e.g., Athanasiadis et al. 2010; Jaffe et al. 2011; Griffin et al. 2017) are broadened to the cool season (Sep–May) and a two-dimensional phase diagram, hereafter referred to as the NPJ Phase Diagram, is developed employing the two leading modes of NPJ variability during that time period. The NPJ Phase Diagram subsequently assists in visualizing the state and evolution of the upper-tropospheric flow pattern over the North Pacific, and serves as an objective tool from which new insights can be derived regarding the climatology and forecast skill of each NPJ regime.

The remainder of this manuscript is structured as follows. Section 2 discusses the development of the NPJ Phase Diagram. Section 3 discusses the climatology of each NPJ regime and reviews the large-scale flow patterns associated with each NPJ regime. Section 4 examines the forecast skill of each NPJ regime in the context of the NPJ Phase Diagram. Section 5 illuminates the characteristics of the best and worst forecast periods in the context of the NPJ Phase Diagram, and Section 6 offers a discussion of the results and some conclusions.

2. Development of the NPJ Phase Diagram

The NPJ Phase Diagram is developed employing anomalies of the zonal component of the 250-hPa vector wind from the 0.5°-resolution National Centers for Environmental Prediction Climate Forecast System Reanalysis (CFSR; Saha et al. 2010, 2014) at 6-h intervals during September–May 1979–2014. Anomalies are calculated as the deviation of the instantaneous 250-hPa zonal wind from a 21-day running mean centered on each analysis time in order to remove the 36-year mean as well as the annual and diurnal cycles. The CFSR is specifically chosen for this study due to its role in providing the initial conditions for the Global Ensemble Forecast System (GEFS) Reforecast Version 2 dataset prior to 2011 (Hamill et al. 2013). The GEFS Reforecast dataset is utilized in Sections 4 and 5 to examine the forecast skill of each NPJ regime in the context of the NPJ Phase Diagram. A traditional EOF analysis (Wilks 2011) is subsequently performed on the 250-hPa zonal wind anomaly data within a horizontal domain bounded in latitude from 10–80°N and in longitude from 100°E–120°W in order to identify the two leading modes of NPJ variability[2].

In comparison to traditional EOF analysis, Griffin and Martin (2017) demonstrate that time-extended EOF analysis of 250-hPa zonal wind anomalies over the North Pacific is beneficial for ensuring that the evolution of the NPJ is characterized by a higher degree of temporal coherence. However, this degree of temporal coherence is achieved by filtering out the high-frequency variability of the NPJ that occurs on daily timescales (Griffin and Martin 2017; their Fig. 1). When considering the NPJ and its influence on the downstream upper-tropospheric flow pattern over North America, short-term fluctuations in the position, intensity, and evolution of the NPJ, such as those associated with recurving tropical cyclones or extratropical

[2] This spatial domain is chosen to match that employed by Griffin and Martin (2017) in their time-extended EOF analysis of 250-hPa zonal wind over the North Pacific.

cyclogenesis, can have substantial impacts on the character of the downstream upper-tropospheric flow pattern over North America (e.g., Torn and Hakim 2015; Archambault et al. 2015; Grams and Archambault 2016). Additionally, the application of time-extended EOF analysis is computationally more expensive than traditional EOF analysis, especially when employing a dataset with 0.5° resolution such as the CFSR. For these two reasons, traditional EOF analysis is chosen for this particular study. The subsequent analysis demonstrates that the application of traditional EOF analysis to 250-hPa zonal wind anomalies during the cool season from the CFSR produces the same two leading modes of NPJ variability as found in previous studies (Athanasiadis et al. 2010; Jaffe et al. 2011; Griffin and Martin 2017).

The regression of 250-hPa zonal wind anomalies from the CFSR onto the two leading spatial patterns obtained from the traditional EOF analysis, EOF 1 and EOF 2, are illustrated in Fig. 1. The sign of a particular EOF pattern is subjective, but is chosen in Fig. 1 to ensure consistency with previous studies on NPJ variability. EOF 1 explains 12.2% of the variance of 250-hPa zonal wind over the North Pacific and corresponds to longitudinal variability of the 250-hPa zonal wind along the axis of the climatological NPJ. A positive EOF 1 pattern (+EOF 1) is associated with a zonal extension of the climatological exit region of the NPJ, while a negative EOF 1 pattern (–EOF 1) is associated with a retraction of the climatological exit region of the NPJ. EOF 2 explains 8.8% of the variance of 250-hPa zonal wind over the North Pacific and corresponds to latitudinal variability of the 250-hPa zonal wind in the vicinity of the exit region of the climatological NPJ. A positive EOF 2 pattern (+EOF 2) is associated with a poleward shift of the exit region of the climatological NPJ, while a negative EOF 2 pattern (–EOF 2) is associated with an equatorward shift of the exit region of the climatological NPJ. The combined variance explained by EOF 1 and EOF 2 is comparable to that found in previous studies

(Athanasiadis et al. 2010; Jaffe et al. 2011; Griffin and Martin 2017) and the two leading EOFs are well separated using the methodology outlined in North et al. (1982). To ensure that the EOF patterns shown in Fig. 1 are representative of the entire cool season, separate traditional EOF analyses were performed on three-month subsets of the 250-hPa zonal wind anomaly data. While not shown, these independent EOF analyses confirm that EOF 1 and EOF 2 represent the two leading modes of NPJ variability with fidelity throughout the cool season.

The 250-hPa zonal wind anomalies at any particular analysis time can be regressed onto EOF 1 and EOF 2 to calculate the instantaneous principal components (PCs), PC 1 and PC 2, that correspond to that analysis time. The magnitude and sign of PC 1 and PC 2 are standardized for ease of interpretation and provide an indication as to how strongly the instantaneous 250-hPa zonal wind anomalies project onto EOF 1 and EOF 2, respectively. Time series constructed from the instantaneous PCs subsequently assist in characterizing the temporal evolution of the NPJ in the context of EOF 1 and EOF 2. As noted by Griffin and Martin (2017), the use of instantaneous PCs produces a noisy time series due to the high-frequency variability that characterizes the NPJ on daily timescales (their Fig. 1). Consequently, in an attempt to describe the evolution of the NPJ with greater temporal coherence while preserving the high-frequency variability of the NPJ on daily timescales, the instantaneous PCs are smoothed through the calculation of a weighted average of the instantaneous PCs within ±24 h of each analysis time, t_0. The specific weight, w, prescribed to the instantaneous PCs at each analysis time, t, within ±24 h of t_0 is defined in accordance with Eq. 1:

$$w = 5 - |t - t_0|/6 \qquad \text{for } |t - t_0| \leq 24 \text{ h} \tag{1}$$

The weighted PCs at a particular analysis time can then be plotted on a two-dimensional Cartesian grid (i.e., the NPJ Phase Diagram) in an effort to visualize the state of the NPJ. The position along the abscissa within the NPJ Phase Diagram corresponds to the value of weighted PC 1 and indicates how strongly the 250-hPa zonal wind anomalies project onto EOF 1. For example, positive values for weighted PC 1 represent a jet extension and negative values represent a jet retraction. The position along the ordinate within the NPJ Phase Diagram corresponds to the value of weighted PC 2 and indicates how strongly the 250-hPa zonal wind anomalies project onto EOF 2. In this sense, positive values of weighted PC 2 represent a poleward shift of the exit region of the climatological NPJ and negative values represent an equatorward shift. Salient examples of NPJ configurations that project strongly onto EOF 1 and EOF 2 are provided in Fig. 2 and Fig. 3, respectively.

As for the sample cases shown in Figs. 2–3, the weighted PCs at all analysis times during September–May 1979–2014 are plotted on the NPJ Phase Diagram in order to classify each analysis time into one of the four NPJ regimes, or to identify analysis times during which the NPJ lies within the unit circle (Fig. 4). For this classification scheme, the analysis times are classified based on, first, whether the position of the NPJ within the NPJ Phase Diagram is greater than a distance of 1 PC unit from the origin and, secondly, whether the absolute value of PC 1 or PC 2 is greater. Analysis times that fall into the "origin" category are interpreted as times during which the NPJ exhibits a neutral signal in the context of the NPJ Phase Diagram.

3. Characteristics of the NPJ Phase Diagram

The classification of analysis times discussed above illuminates several salient characteristics that can be prescribed to each NPJ regime. The typical residence time of the NPJ within each NPJ regime is provided in Table 1. Overall, the mean and median residence time within an NPJ regime do not vary considerably among the NPJ regimes. Specifically, the mean residence time within an NPJ regime ranges between 3.58–3.85 days, while the median residence time ranges between 2.50–2.75 days. The residence time is slightly longer for periods when the NPJ resides within the unit circle, however, with a mean and median residence time of 4.65 days and 3.25 days, respectively. Consideration of the minimum and maximum residence time within each NPJ regime also indicates that an NPJ regime can be transient or may persist for multiple weeks.

As demonstrated from previous studies on NPJ variability, each NPJ regime exhibits a strong influence on the character of the downstream large-scale flow pattern over North America (e.g., Athanasiadis et al. 2010; Jaffe et al. 2011; Griffin and Martin 2017). To ensure consistency with previous work, composite analyses are constructed employing the CFSR for periods during which the NPJ resided within the same NPJ regime for at least three consecutive days. A three-day threshold is chosen as a compromise between the magnitude of the mean and median residence time for each NPJ regime (Table 1). Figures 5 and 6 illustrate the characteristic large-scale flow pattern four days following the onset of each NPJ regime. This particular time is chosen subjectively for brevity and to highlight both the characteristic structure of the NPJ, as well as the downstream flow pattern over North America associated with each NPJ regime. Two-sided Student's t-tests were performed on the geopotential height and temperature anomaly fields shown in Figs. 5–6 to identify anomalies that are statistically significant at the 99% confidence interval. The reader is referred to Griffin and Martin (2017) for greater detail on the evolution of the large-scale flow pattern associated with each NPJ regime.

A jet extension is characterized by the meridional juxtaposition of an anomalous upper-tropospheric trough over the central North Pacific and an anomalous ridge over the subtropical North Pacific that combine to produce a strong, zonally-oriented NPJ (Fig. 5a). Beneath the left-exit region of the extended NPJ, an anomalous surface cyclone drives anomalous southerly geostrophic flow along the west coast of North America (Fig. 6a). This southerly geostrophic flow is associated with the development of lower-tropospheric warm anomalies over western North America and the amplification of an anomalous upper-tropospheric ridge in that location, as well (Fig. 5a). Lower-tropospheric cold anomalies are found upstream of the surface cyclone in conjunction with anomalous northerly geostrophic flow in that location, and across eastern North America beneath an anomalous upper-tropospheric trough (Fig. 6a).

A jet retraction features an anomalous upper-tropospheric ridge over the central North Pacific, and anomalous troughs over northwestern North America and the subtropical North Pacific (Fig. 5b). In combination, these geopotential height anomalies result in a compact NPJ over the western North Pacific and a split NPJ to the east of the date line. Directly beneath the upper-tropospheric ridge over the central North Pacific, the circulation associated with an anomalous surface anticyclone contributes to the development of lower-tropospheric cold anomalies over Alaska and the west coast of North America, and warm anomalies over the central North Pacific (Fig. 6b). Lower-tropospheric warm anomalies are also found in the south central U.S. upstream of an anomalous upper-tropospheric ridge over the southeastern U.S.

A poleward shift exhibits an anomalous upper-tropospheric trough over the high-latitude North Pacific and an anomalous ridge over the subtropical North Pacific that act in combination to shift the exit region of the NPJ poleward of 40°N (Fig. 5c). An anomalous surface cyclone is located beneath the left-exit region of the poleward-shifted NPJ, which results in anomalous southerly geostrophic flow over northern North America and the development of lower-tropospheric warm anomalies in that location (Fig. 6c). These lower-tropospheric warm anomalies are also associated with an anomalous upper-tropospheric ridge positioned over eastern Canada (Fig. 5c). Lower-tropospheric cold anomalies are only observed in the composite over the Bering Strait and Gulf of Alaska during a poleward shift in conjunction with anomalous northerly geostrophic flow upstream of the surface cyclone (Fig. 6c).

Lastly, an equatorward shift is associated with an anomalous upper-tropospheric ridge over the high-latitude North Pacific and an anomalous trough over the subtropical North Pacific, reminiscent of a Rex block (Fig. 5d; Rex 1950). This configuration of geopotential height anomalies results in an equatorward deflection of the exit region of the NPJ near Hawaii, and a weaker NPJ over the western North Pacific compared to the other NPJ regimes. An anomalous upper-tropospheric trough is also positioned over eastern Canada downstream of the high-latitude ridge over the North Pacific (Fig. 5d). In the lower-troposphere, an equatorward shift is associated with an anomalous surface anticyclone centered near the Aleutian Islands. This surface anticyclone facilitates anomalous northerly geostrophic flow over northern North America and the development of lower-tropospheric cold anomalies in that location (Fig. 6d). Conversely, anomalous southerly geostrophic flow upstream of the surface anticyclone contributes to the development of lower-tropospheric warm anomalies over the Bering Strait and the Gulf of Alaska.

Further insight is found by considering the interannual and intraannual variability of each NPJ regime. While the NPJ resides within one of the four NPJ regimes 59% of the time during a typical cool season (not shown), there is considerable interannual variability in the frequency of each NPJ regime (Fig. 7a). As an example, the 1997–1998 cool season was characterized by the second-lowest annual frequency of poleward shifts (4.7%), while the subsequent 1998–1999 cool season featured highest annual frequency of poleward shifts (34.9%). Comparable abrupt changes in the annual frequency of an individual NPJ regime are readily observed when considering the time series for other NPJ regimes, as well. Furthermore, linear regressions performed on each of the time series shown in Fig. 7a identify no statistically significant trends in the frequency of each NPJ regime during 1979–2014 (not shown).

Substantial variability characterizes the frequency of each NPJ regime throughout the duration of an individual cool season, as well (Fig. 7b). Specifically, the NPJ resides within an NPJ regime most frequently during November–March and less frequently during the months of September, October, April, and May. Both jet extensions and jet retractions peak in frequency during the month of March, while poleward shifts and equatorward shifts peak during February and January, respectively. The frequencies of each NPJ regime during an individual month are generally comparable, except during March, when jet extensions and jet retractions are noticeably more frequent than poleward shifts and equatorward shifts, and during September, when poleward shifts and equatorward shifts are nearly two times more frequent than jet extensions and jet retractions.

As may be anticipated, the interannual and intraannual frequency of each NPJ regime are strongly modulated by large-scale atmospheric teleconnection patterns. For example, the Pacific/North American (PNA) pattern is known to exhibit a strong relationship with the intensity of the NPJ (e.g., Wallace and Gutzler 1981; Barnston and Livesey 1987; Franzke and Feldstein 2005; Strong and Davis 2008; Athanasiadis et al. 2010; Franzke et al. 2011; Griffin and Martin 2017). Specifically, a positive PNA pattern is canonically characterized by an anomalous upper-tropospheric trough over the central North Pacific and an anomalous ridge over the subtropical North Pacific. Consequently, a positive PNA pattern is particularly conducive to the development of an extended NPJ. Conversely, a negative PNA pattern exhibits an anomalous upper-tropospheric ridge over the central North Pacific that favors a retracted NPJ.

To clearly illustrate the relationship between the PNA and each NPJ regime, all analysis times that were characterized by a NPJ regime were classified based on the sign and magnitude of the daily PNA index (CPC 2017a). Analysis times that featured a PNA index > 0.5 were classified as occurring during a positive PNA, those that featured a PNA index < –0.5 were classified as occurring during a negative PNA, and those remaining were classified as occurring during a neutral PNA. Figure 8a demonstrates that the frequency of each NPJ regime is indeed well associated with the phase of the PNA, with jet extensions and poleward shifts occurring most frequently during a positive PNA, and jet retractions and equatorward shifts occurring most frequently during a negative PNA.

The frequency of each NPJ regime also exhibits an association with the phase of the Arctic Oscillation (AO; Thompson and Wallace 1998; Higgins et al. 2000; Ambaum et al. 2001). The positive phase of the AO is canonically characterized by above-normal 1000-hPa geopotential heights over the central North Pacific and below-normal 1000-hPa geopotential heights over the Arctic. As for the PNA index, daily AO indices (CPC 2017b) are employed to classify analysis times that were characterized by a NPJ regime. Those analysis times exhibiting an AO index > 0.5 were classified as occurring during a positive AO, those exhibiting an AO index < –0.5 were classified as occurring during a negative AO, and those remaining were classified as occurring during a neutral AO. Figure 8b indicates that jet retractions are most frequent during a positive AO and jet extensions are most frequent during a negative AO. This relationship agrees with the NPJ regime composites shown in Fig. 6, given that jet retractions are associated with an anomalous surface anticyclone over the central North Pacific (Fig. 6b), and jet extensions feature an anomalous surface cyclone in that location (Fig. 6a).

The El Niño–Southern Oscillation (ENSO) can also modulate the configuration of the

NPJ. For example, prior work suggests that anomalous convection and above-normal sea-surface temperatures over the central and eastern equatorial Pacific during an El Niño favor an extended and equatorward-shifted NPJ. Conversely, anomalous convection and above-normal sea-surface temperatures over the western equatorial Pacific during a La Niña favor a retracted NPJ (e.g., Horel and Wallace 1981; Rasmusson and Wallace 1983; Rasmusson and Mo 1993; Yang et al. 2002; Xie et al. 2015; Cook et al. 2017). In an effort to frame this relationship in the context of the NPJ Phase Diagram, analysis times that were characterized by a NPJ regime were classified based on the sign and magnitude of the monthly Nino3.4 index (ESRL 2017). Any analysis times that coincided with a Nino3.4 index > 1.0 were classified as occurring during an El Niño, analysis times that coincided with a Nino3.4 index < –1.0 were classified as occurring during a La Niña, and all other analysis times were classified as occurring during a neutral ENSO state. Figure 8c demonstrates that El Niño is indeed characterized by a higher frequency of jet extensions and equatorward shifts. Conversely, La Niña is characterized by a higher frequency of jet retractions and poleward shifts. The results from Fig. 8c translate to individual cool seasons characterized by El Niño and La Niña events, as well. For example, Fig. 7a indicates that the 1982–1983 El Niño cool season (Sep–May Nino3.4 = 1.82) featured a higher frequency of jet extensions and equatorward shifts, while the 1999–2000 La Niña cool season (Sep–May Nino3.4 = –1.22) featured a higher frequency of jet retractions and poleward shifts.

4. GEFS Forecast Skill in the Context of the NPJ Phase Diagram

Provided with a relationship between each NPJ regime and the downstream large-scale flow pattern over North America, complementary knowledge of the forecast skill associated with each NPJ regime offers the potential to increase confidence in operational medium-range forecasts over North America. To evaluate the forecast skill associated with each NPJ regime, an ensemble of 9-day forecast trajectories within the NPJ Phase Diagram are calculated daily during September–May 1985–2014 using 250-hPa zonal wind data from the 1.0°-resolution GEFS Reforecast Version 2 dataset (Hamill et al. 2013). The GEFS Reforecast dataset features 10 ensemble member forecasts and 1 control member forecast initialized daily at 0000 UTC, each with forecast lead times as long as 384 h.

Forecast errors within the NPJ Phase Diagram are calculated as the distance error in PC units between the ensemble mean NPJ Phase Diagram forecast and the verifying 0-h analysis that corresponds to each forecast lead time. The NPJ Phase Diagram forecasts are then classified (1) based on the position of the NPJ within the NPJ Phase Diagram at the time of forecast initialization or forecast verification, following the schematic shown in Fig. 4, and (2) based on season. Two-sided Student's t-tests are performed on all NPJ Phase Diagram forecast error statistics to indicate statistical significance in accordance with the criteria outlined in each pertinent figure caption.

The average distance errors associated with ensemble mean NPJ Phase Diagram forecasts that initialize during the same season are provided in Fig. 9a. Overall, NPJ Phase Diagram forecasts that initialize during the winter (Dec–Feb) exhibit significantly larger distance errors within the NPJ Phase Diagram than forecasts that initialize during the fall (Sep–Nov) and spring (Mar–May) at forecast lead times less than 144 h. At lead times longer than 144 h, forecasts that initialize during the winter and spring exhibit significantly larger distance errors than forecasts that initialize during the fall. Furthermore, forecasts that initialize during the fall exhibit distance errors that fall below the cool-season average at all forecast lead times, while forecasts that initialize during the winter exhibit errors that lie above the cool-season average at all forecast lead times.

The average distance errors of ensemble mean NPJ Phase Diagram forecasts that initialize during the same NPJ regime are shown in Fig. 9b. At lead times less than 120 h, no significant differences in distance error are observed between the NPJ regimes. However, significant differences between the NPJ regimes begin to emerge at lead times longer than 120 h. Specifically, forecasts that initialize during a jet retraction exhibit significantly larger distance errors than forecasts that initialize during a poleward shift at lead times between 120–168 h, and significantly larger distance errors than forecasts that initialize during a jet extension at lead times between 192–216 h. However, despite these significant differences at lead times longer than 120 h, the spread in distance errors between the NPJ regimes is generally less than 0.10 PC units during this time frame. Substantially larger spread between the distance errors associated with each NPJ regime is found while considering NPJ Phase Diagram forecasts that verify during the same NPJ regime (Fig. 9c). In particular, forecasts that verify during equatorward shifts and jet retractions exhibit significantly larger distance errors than poleward shifts and jet extensions at lead times greater than 96 h. Consequently, knowledge of the NPJ regime at the time of forecast verification appears to be a greater indicator of forecast skill in the context of the NPJ Phase Diagram than the NPJ regime at the time of forecast initialization.

The poor forecast skill of ensemble mean NPJ Phase Diagram forecasts that verify during equatorward shifts is also apparent when considering the frequency with which each NPJ regime is overforecast or underforecast in the GEFS Reforecast dataset. Figure 10 demonstrates that, compared to the verifying 0-h analysis, equatorward shifts are substantially underforecast by ensemble mean NPJ Phase Diagram forecasts at all lead times. Specifically, equatorward shifts are underforecast by nearly 26% at a 216-h lead time, which is at least double the frequency that the other NPJ regimes are underforecast at that same lead time. While all NPJ regimes are generally underforecast by the ensemble mean NPJ Phase Diagram forecasts at lead times greater than 168 h, both jet extensions and poleward shifts are overforecast at lead times less than 168 h.

5. Best and Worst NPJ Phase Diagram Forecasts

Additional insight into the forecast skill associated with each NPJ regime is found by considering the characteristics of the best and worst NPJ Phase Diagram medium-range forecasts. Such an investigation has the potential to illuminate factors that may contribute to reduced or enhanced forecast skill (e.g., Lillo and Parsons 2017). The best and worst medium-range forecasts in the context of the NPJ Phase Diagram are identified as those forecasts that rank in the top or bottom 10%, respectively, in terms of both (1) the average GEFS ensemble *mean* distance error of the 192- and 216-h forecasts and (2) the average GEFS ensemble *member* distance error of the 192- and 216-h forecasts. The first criterion provides a measure of forecast accuracy during the medium-range period, while the second criterion provides a measure of forecast precision during the medium-range period.

Figure 11 illustrates a series of hypothetical NPJ Phase Diagram forecasts that would qualify as a best, an intermediate, and a worst forecast in the context of the two criteria listed above. A best forecast is one in which the ensemble mean forecast exhibits a small distance error, as well as a small average ensemble member distance error. Consequently, a best forecast can be interpreted as one in which the NPJ Phase Diagram forecast is both accurate and precise. The intermediate forecast depicts a situation in which there is a small ensemble mean distance error, but also a large average ensemble member distance error. Consequently, both criteria are not satisfied, and this situation represents one in which the forecast was accurate but not particularly precise. Finally, a worst forecast is a situation that exhibits large ensemble mean distance error and large average ensemble member distance error, or a forecast that was neither accurate nor precise.

As a whole, the frequency distribution of the worst NPJ Phase Diagram forecasts features two separate maxima during the cool season, one during December and a second during February–April, with a relative minimum during January (Fig. 12a). The best NPJ Phase Diagram forecasts tend to occur most frequently during the beginning and end of the cool season, but also peak during December. The best and worst NPJ Phase Diagram forecasts are classified based on the NPJ regime at the time of forecast initialization in Fig. 12b. This frequency distribution indicates that the worst forecasts are initialized disproportionately more during jet retractions and equatorward shifts, while the best forecasts are initialized disproportionately more during jet extensions and poleward shifts. The average value of PC 1 and PC 2 at the time of forecast initialization also indicates a preference for the worst forecasts to initialize more frequently during jet retractions and equatorward shifts, and for the best forecasts to initialize more frequently during jet extensions and poleward shifts (Table 2). However, only the values of PC 1 are statistically different between the best and worst forecasts at the time of forecast initialization.

The evolution of the NPJ during the 10-day period following the initialization of a best or worst NPJ Phase Diagram forecast also differs substantially. In particular, the average change in PC 2 during the 10-day period following a worst forecast indicates a significant movement towards an equatorward shift within the NPJ Phase Diagram, while the 10-day period following a best forecast exhibits a significant movement towards a poleward shift. Additionally, the worst forecast periods also feature significantly longer trajectories within the NPJ Phase Diagram compared to the best forecast periods during the 10 days that follow forecast initialization. This particular result suggests that the worst forecasts often occur during periods characterized by rapid NPJ regime change, while the best forecast periods are characterized by more persistent upper-tropospheric flow patterns over the North Pacific. This result aligns well with previous work that suggests periods characterized by upper-tropospheric regime change are associated with reduced forecast skill (e.g., Tibaldi and Molteni 1990; Frederiksen et al. 2004; Pelly and Hoskins 2006; Ferranti et al. 2015; Lillo and Parsons 2017).

An examination of the upper-tropospheric flow patterns associated with the best and worst forecast periods also offers insight into the types of synoptic flow patterns that are associated with enhanced or reduced forecast skill. This examination is performed by employing the CFSR to construct composite analyses of 250-hPa wind speed, geopotential height, and geopotential height anomalies at the time a best or worst forecast is initialized, as well as at 192 h following forecast initialization. Two-sided Student's t-tests are subsequently used to evaluate whether the difference between geopotential height anomalies associated with the worst and best forecast composites is statistically significant at each time period.

The composite upper-tropospheric flow patterns at the time a best or worst forecast is initialized within each NPJ regime are provided in Fig. 13. At first glance, an examination of the geopotential height anomalies associated with each composite reveals few qualitative differences between the best and worst forecasts initialized during the same NPJ regime. However, closer scrutiny reveals some significant differences. In particular, while both the best and worst forecasts initialized during a jet extension are characterized by a strong, zonally-extended NPJ at the time of forecast initialization (Figs. 13a,b), the worst forecasts exhibit significantly higher geopotential heights over the eastern North Pacific compared to the best forecasts (Fig. 14a). Similarly, both the best and worst forecasts initialized during a jet retraction feature an anomalous ridge over the central North Pacific (Figs. 13c,d). However, the worst forecasts exhibit statistically larger geopotential height anomalies over the Gulf of Alaska, and statistically lower geopotential height anomalies over the subtropical North Pacific and the western Great Lakes (Fig. 14b). The lower geopotential height anomalies over the subtropical North Pacific and western Great Lakes exhibited by the worst forecasts also favor a stronger southern stream of the NPJ to the east of the date line and less pronounced ridging over eastern North America when compared to the best forecasts (Figs. 13c,d).

As during jet extensions and jet retractions, the worst forecasts initialized during a poleward shift also exhibit significantly higher geopotential height anomalies over the Gulf of Alaska compared to the best forecasts (Figs. 13e,13f,14c). The worst forecasts initialized during a poleward shift are also characterized by a more intense NPJ, a stronger jet stream over North America, and significantly lower geopotential height anomalies over the southwestern U.S. and northwestern Mexico. (Figs. 13e,13f,14c). While not as prominent as in other composites, the worst forecasts initialized during an equatorward shift also exhibit significantly larger geopotential height anomalies over the eastern North Pacific compared to the best forecasts (Figs. 13g,13h,14d). Consequently, the presence of larger geopotential height anomalies over the eastern North Pacific at the time of forecast initialization is a noticeable differentiator between the worst and best forecasts regardless of the prevailing NPJ regime.

More substantial differences in the upper-tropospheric flow pattern over the North Pacific are observed 192 h following the initialization of a best and worst forecast. In particular, the upper-tropospheric flow pattern 192 h following the initialization of a best forecast is characterized by an anomalous trough over the high-latitude North Pacific and an anomalous ridge over the subtropical North Pacific that, in combination, favor an extended and poleward-shifted NPJ regardless of the NPJ regime at the time of forecast initialization (Figs. 15a,c,e,g). Downstream of the trough over the high-latitude North Pacific, an anomalous ridge is also firmly positioned over North America in the best forecast composites. In contrast, the upper-tropospheric flow pattern 192 h following the initialization of a worst forecast features an anomalous ridge over the high-latitude North Pacific and a retracted NPJ regardless of the NPJ regime at the time of forecast initialization (Figs. 15b,d,f,h). An anomalous trough of variable strength is also located over North America in all of the worst forecast composites, downstream of the high-latitude North Pacific ridge.

The difference between the geopotential height anomalies 192 h following the initialization of a worst and best forecast are clearly identified in Fig. 16. Compared to the best forecast composites, the worst forecast composites exhibit significantly higher geopotential height anomalies at high latitudes over the North Pacific, and significantly lower geopotential height anomalies over the subtropical North Pacific, reminiscent of a Rex block (Rex 1950). Notably, this difference pattern prevails regardless of the NPJ regime at the time of forecast initialization. Consequently, the upper-tropospheric flow patterns shown in Fig. 13 and Fig. 15 uniformly suggest that periods characterized by the development and/or maintenance of upper-tropospheric blocking events over the North Pacific are associated with the worst forecast skill in the context of the NPJ Phase Diagram. Conversely, those periods that evolve towards a zonal flow pattern over the North Pacific are generally associated with enhanced forecast skill.

6. Discussion and Conclusions

The preceding analysis corroborates the results from prior studies of NPJ variability that establish a clear connection between the two leading modes of 250-hPa zonal wind variability over the North Pacific and the large-scale flow pattern over North America (e.g., Athanasiadis et al. 2010; Jaffe et al. 2011; Griffin and Martin 2017). Provided with this connection, this study utilizes the two leading modes of 250-hPa zonal wind variability from the CFSR during the cool season as the foundation for developing the NPJ Phase Diagram. The NPJ Phase Diagram subsequently provides an objective tool to monitor the state and evolution of the upper-tropospheric flow pattern over the North Pacific, to identify the prevailing NPJ regime, and to evaluate the characteristic forecast skill associated with each NPJ regime.

The application of the NPJ Phase Diagram to 250-hPa zonal wind data from the CFSR during September–May 1979–2014 illuminates several salient characteristics of each NPJ regime and highlights opportunities for future research. In particular, while the mean and median residence times within a particular NPJ regime are typically on the order of three days, a NPJ regime can persist for multiple weeks. Furthermore, it is apparent that the frequency of each NPJ regime exhibits considerable interannual and intraannual variability. Given the relationship between each NPJ regime and the large-scale flow pattern over North America, further investigation into the synoptic flow patterns that are conducive to prolonged residence times within a NPJ regime, or that increase the frequency of a NPJ regime, may offer considerable value to operational seasonal and subseasonal forecasts over North America.

Large-scale atmospheric teleconnection patterns can strongly modulate the frequency of each NPJ regime. For example, it was noted that a positive (negative) PNA is characterized by an increased frequency of jet extensions and poleward shifts (jet retractions and equatorward shifts). However, recall from Figs. 6a,c that jet extensions and poleward shifts are associated with distinctly different lower-tropospheric temperature anomalies over North America, with jet extensions favoring anomalously cold temperatures over eastern North America and poleward shifts favoring anomalously warm temperatures over northern North America. Consequently, knowledge of the prevailing NPJ regime provides additional operational value beyond sole knowledge of the PNA index when evaluating the character of the large-scale flow pattern over North America. The NPJ Phase Diagram provides an objective basis for detailed investigations of NPJ variability during other well-established atmospheric teleconnection patterns, as well, such as the AO, ENSO, North Atlantic Oscillation (e.g., Wallace and Gutzler 1981), and Madden–Julian Oscillation (Madden and Julian 1972). Such investigations may offer additional value to seasonal and subseasonal forecasts by illuminating the palette of synoptic-scale flow evolutions over the North Pacific that may operate during a particular atmospheric teleconnection pattern.

Knowledge of the relative forecast skill associated with each NPJ regime illuminates particular periods during the cool season that may be characterized by reduced or enhanced forecast skill. In particular, the frequency distribution of worst forecasts in the context of the NPJ Phase Diagram exhibits a bimodal structure throughout the duration of an individual cool season, with relative maxima during December and March, and a relative minimum during January. While it is clear that ensemble mean forecasts initialized during the winter generally exhibit the largest distance errors within the NPJ Phase Diagram, additional research is necessary to affirm the veracity of the relative frequency minimum that characterizes the worst NPJ Phase Diagram forecasts during January and to identify factors that may contribute to its occurrence.

Examination of the forecast skill associated with each NPJ regime offers additional insight into the types of synoptic flow patterns that exhibit reduced forecast skill. Overall, the analysis persistently indicates that forecasts that verify during jet retractions and equatorward shifts exhibit reduced forecast skill in the context of the NPJ Phase Diagram compared to jet extensions and poleward shifts. Recall from the NPJ composites in Figs. 5–6, that these particular NPJ regimes are associated with the development of anomalous ridges in the central and high-latitude North Pacific, respectively. In light of this observation, it is likely that diabatic processes account for some of the reduced forecast skill associated with these NPJ regimes, given the established ability of diabatic processes to amplify the flow pattern, (e.g., Massacand et al. 2001; Riemer et al. 2008; Torn 2010; Ferranti et al. 2015; Pfahl et al. 2015; Grams and Archambault 2016). Additional case study work that utilizes the NPJ Phase Diagram to interrogate poor forecasts that verify within jet retractions and equatorward shifts is likely to illuminate the specific processes that contribute to the reduced forecast skill during these NPJ regimes.

An examination of the worst and best medium-range forecasts in the context of the NPJ Phase Diagram suggests that the worst forecasts are associated with the development or persistence of upper-tropospheric blocking events over the North Pacific. This result holds regardless of the NPJ regime at the time of forecast initialization, and corroborates previous work highlighting the reduced predictability associated with the development of upper-tropospheric blocking events (e.g., Tibaldi and Molteni 1990; D'Andrea et al. 1998; Frederiksen et al. 2004; Pelly and Hoskins 2006; Matsueda 2011; Ferranti et al. 2015). Consequently, greater understanding surrounding the variability of flow evolutions that are conducive to the development of upper-tropospheric blocking events is necessary. The NPJ Phase Diagram provides an objective frame of reference from which to examine the development of upper-tropospheric blocking events and to identify the spectrum of synoptic flow evolutions that are conducive to block formation. Additionally, it is apparent that the worst forecasts are associated with a significant movement towards an equatorward shift within the NPJ Phase Diagram during the 10-day period following forecast initialization, while the best forecasts exhibit a significant movement towards a poleward shift. In light of this result, the NPJ Phase Diagram provides an objective tool to identify NPJ regime transitions and can be utilized to examine the characteristic synoptic flow patterns associated with those transitions. Results from such examinations have the potential to increase confidence in operational forecasts during periods of regime transition, given that certain trajectories within the NPJ Phase Diagram are associated with reduced forecast skill.

Finally, the relative forecast skill associated with each NPJ regime is only applicable in the context of the GEFS Reforecast dataset. Consequently, additional research is required to evaluate the forecast skill of NPJ regimes in the context of other global prediction systems. An independent evaluation of forecast skill in the context of these other global prediction systems has the potential to illuminate whether the large-scale flow patterns that exhibit reduced skill in the GEFS Reforecast dataset are pervasive across all modeling systems. To the degree that any differences exist between global prediction systems with respect to the relative forecast skill of NPJ regimes, these evaluations have the potential to identify situations during which greater confidence could be prescribed to a particular global prediction system.

Acknowledgments

The authors thank Mike Bodner, Daniel Halperin, Arlene Laing, Bill Lamberson, Sara Ganetis, and Josh Kastman for their constructive discussions concerning the NPJ Phase Diagram. The authors also thank the National Oceanic and Atmospheric Administration for its support of this work via grant NA15NWS4680006.

References

Ambaum, M., B. Hoskins, and D. Stephenson, 2001: Arctic Oscillation or North Atlantic Oscillation? *J. Climate*, **14**, 3495–3507, doi: https://doi.org/10.1175/1520-0442(2001)014<3495:AOONAO>2.0.CO;2.

Archambault, H. M., L. F. Bosart, D. Keyser, and J. M. Cordeira, 2013: A climatological analysis of the extratropical flow response to recurving western North Pacific tropical cyclones. *Mon. Wea. Rev.*, **141**, 2325–2346, doi: https://doi.org/10.1175/MWR-D-12-00257.1.

Archambault, H. M., D. Keyser, L. F. Bosart, C. A. Davis, and J. M. Cordeira, 2015: A composite perspective of the extratropical flow response to recurving western North Pacific tropical cyclones. *Mon. Wea. Rev.*, **143**, 1122–1141, doi: https://doi.org/10.1175/MWR-D-14-00270.1.

Athanasiadis, P. J., J. M. Wallace, and J. J. Wettstein, 2010: Patterns of wintertime jet stream variability and their relation to the storm tracks. *J. Atmos. Sci.*, **67**, 1361–1381, doi: https://doi.org/10.1175/2009JAS3270.1.

Barnston, A. G., and R. E. Livezey, 1987: Classification, seasonality and persistence of low-frequency atmospheric circulation patterns. *Mon. Wea. Rev.*, **115**, 1083–1126.

Chang, E. K. M., S. Lee, and K. L. Swanson, 2002: Storm track dynamics. *J. Climate*, **15**, 2163–2183, doi: https://doi.org/10.1175/1520-0442(2002)015<02163:STD>2.0.CO;2.

Cook, A. R., L. M. Leslie, D. B. Parsons, and J. T. Schaefer, 2017: The impact of El Niño–Southern Oscillation (ENSO) on winter and early spring U.S. tornado outbreaks. *J. Appl. Meteor. Climatol.*, **56**, 2455–2478, doi: https://doi.org/10.1175/JAMC-D-16-0249.1.

CPC, 2017a: Pacific/North American pattern. Accessed 9 February 2017, http://www.cpc.ncep.noaa.gov/products/precip/CWlink/pna/pna.shtml.

CPC, 2017b: Arctic Oscillation. Accessed 9 February 2017, http://www.cpc.ncep.noaa.gov/products/precip/CWlink/daily_ao_index/ao.shtml.

D'Andrea, F., and Coauthors, 1998: Northern Hemisphere atmospheric blocking as simulated by 15 atmospheric general circulation models in the period 1979–1988. *Climate Dyn.*, **14**, 385–407, doi: https://doi.org/10.1007/s003820050230.

Eichelberger, S. J., and D. L. Hartmann, 2007: Zonal jet structure and the leading mode of variability. *J. Climate*, **20**, 5149–5163, doi: https://doi.org/10.1175/JCLI4279.1.

ESRL, 2017: Niño 3.4 SST Index. Accessed 5 January 2017, https://www.esrl.noaa.gov/psd/gcos_wgsp/Timeseries/Nino34/.

Ferranti, L., S. Corti, and M. Janousek, 2015: Flow-dependent verification of ECMWF ensemble over the Euro-Atlantic sector. *Quart. J. Roy. Meteor. Soc.*, **141**, 916–924, doi: 10.1002/qj.2411.

Franzke, C.S., and S. B. Feldstein, 2005: The continuum and dynamics of Northern Hemisphere teleconnection patterns. *J. Atmos. Sci.*, **62**, 3250–3267.

Franzke, C. S., S. B. Feldstein, and S. Lee, 2011: Synoptic analysis of the Pacific–North America teleconnection pattern. *Quart. J. Roy. Meteor. Soc.*, **137**, 329–346, doi: https://doi.org/10.1002/qj.768.

Frederiksen, J. S., M. A. Collier, and A. B. Watkins, 2004: Ensemble prediction of blocking regime transitions. *Tellus*, **56A**, 485–500.

Grams, C. M., and H. M. Archambault, 2016: The key role of diabatic outflow in amplifying the midlatitude flow: A representative case study of weather systems surrounding western

North Pacific extratropical transition. *Mon. Wea. Rev.*, **144**, 3847–3869, doi: https://doi.org/10.1175/MWR-D-15-0419.1.

Griffin, K. S., and J. E. Martin, 2017: Synoptic features associated with temporally coherent modes of variability of the North Pacific jet stream. *J. Climate*, **30**, 39–54, doi: https://doi.org/10.1175/JCLI-D-15-0833.1.

Hakim, G. J., 2003: Developing wave packets in the North Pacific storm track. *Mon. Wea. Rev.*, **131**, 2824–2837, doi: https://doi.org/10.1175/1520-0493(2003)131<2824:DWPITN>2.0.CO;2.

Harr, P. A., and J. M. Dea, 2009: Downstream development associated with the extratropical transition of tropical cyclones over the western North Pacific. *Mon. Wea. Rev.*, **137**, 1295–1319, doi: https://doi.org/10.1175/2008MWR2558.1.

Hamill, T. M., G. T. Bates, J. S. Whitaker, D. R. Murray, M. Fiorino, T. J. Galarneau Jr., Y. Zhu, and W.Lapenta, 2013: NOAA's second-generation global medium-range ensemble reforecast data set. *Bull. Amer. Meteor. Soc.*, **94**, 1553–1565, doi: https://doi.org/10.1175/BAMS-D-12-00014.1.

Handlos, Z., and J. Martin, 2016: Composite analysis of large-scale environments conducive to West Pacific polar/subtropical jet superposition. *J. Climate*, **29**, 7145–7165, doi: https://doi.org/10.1175/JCLI-D-16-0044.1.

Higgins, R. W., J.-K. E. Schemm, W. Shi, and A. Leetmaa, 2000: Extreme precipitation events in the western United States related to tropical forcing. *J. Climate*, **13**, 793–820, doi: https://doi.org/10.1175/1520-0442(2000)013<0793:EPEITW>2.0.CO;2.

Horel, J. D., and J. M. Wallace, 1981: Planetary-scale atmospheric phenomena associated with the Southern Oscillation. *Mon. Wea. Rev.*, **109**, 813–829, doi: https://doi.org/10.1175/1520-0493(1981)109<0813:PSAPAW>2.0.CO;2.

Hoskins, N. J., and D. J. Karoly, 1981: The steady linear response of a spherical atmosphere to thermal and orographic forcing. *J. Atmos. Sci.*, **38**, 1179–1196, doi: https://doi.org/10.1175/1520-0469(1981)038<1179:TSLROA>2.0.CO;2.

Jaffe, S. C., J. E. Martin, D. J. Vimont, and D. J. Lorenz, 2011: A synoptic climatology of episodic, subseasonal retractions of the Pacific jet. *J. Climate*, **24**, 2846–2860, doi: https://doi.org/10.1175/2010JCLI3995.1.

Jhun, J. G., and E. J. Lee, 2004: A new East Asian winter monsoon index and associated characteristics of the winter monsoon. *J. Climate*, **17**, 711–726, doi: https://doi.org/10.1175/1520-0442(2004)017<0711:ANEAWM>2.0.CO;2.

Kalnay, E., and Coauthors, 1996: The NCEP/NCAR 40-Year Reanalysis Project. *Bull. Amer. Meteor. Soc.*, **77**, 437–471, doi: https://doi.org/10.1175/1520-0477(1996)077<0437:TNYRP>2.0.CO;2.

Lee, Y.-Y., G.-H. Lim, and J.-S. Kug, 2010: Influence of the East Asian winter monsoon on the storm track activity over the North Pacific. *J. Geophys. Res.*, **115**, D09102, doi: https://doi.org/10.1029/2009JD012813.

Lillo, S. P., and D. B. Parsons, 2017: Investigating the dynamics of error growth in ECMWF medium-range forecast busts. *Quart. J. Roy. Meteor. Soc.*, **143**, 1211–1226, doi: 10.1002/qj.2938.

Lin, H., and J. Derome, 1996: Changes in predictability associated with the PNA pattern. *Tellus*, **48A**, 553–571, doi: 10.1034/j.1600-0870.1996.t01-3-00005.x.

Madden, R. A., and P. R. Julian, 1972: Description of global-scale circulation cells in the tropics with a 40–50 day period. *J. Atmos. Sci.*, **29**, 1109–1123, doi: https://doi.org/10.1175/1520-0469(1972)029<1109:DOGSCC>2.0.CO;2.

Madden, R. A., and P. R. Julian, 1994: Observations of the 40–50-day tropical oscillation—A review. *Mon. Wea. Rev.*, **122**, 814–837, doi: https://doi.org/10.1175/1520-0493(1994)122<0814:OOTDTO>2.0.CO;2.

Massacand, A. C., H. Wernli, and H. C. Davies, 2001: Influence of upstream diabatic heating upon an alpine event of heavy precipitation. *Mon. Wea. Rev.*, **129**, 2822–2828, doi: https://doi.org/10.1175/1520-0493(2001)129<2822:IOUDHU>2.0.CO;2.

Matsueda, M., 2011: Predictability of Euro-Russian blocking in summer of 2010. *Geophys. Res. Lett.*, **38**, L06801, doi: https://doi.org/10.1029/2010GL046557.

North, G. R., T. L. Bell, R. F. Cahalan, and F. J. Moeng, 1982: Sampling errors in the estimation of empirical orthogonal functions. *Mon. Wea. Rev.*, **110**, 699–706, doi: https://doi.org/10.1175/1520-0493(1982)110<0699:SEITEO>2.0.CO;2.

Orlanski, I., and J. P. Sheldon, 1995: Stages in the energetics of baroclinic systems. *Tellus*, **47A**, 605–628, doi: https://doi.org/10.1034/j.1600-0870.1995.00108.x.

Palmer, T. N., 1988: Medium and extended range predictability and stability of the Pacific/North American mode. *Quart. J. Roy. Meteor. Soc.*, **114**, 691–713. doi: 10.1002/qj.49711448108.

Pelly J. L., and B. J. Hoskins, 2006: How well does the ECMWF Ensemble Prediction System predict blocking? *Quart. J. Roy. Meteor. Soc.*, **129**, 1683–1702, doi: 10.1256/qj.01.173.

Pfahl, S., C. Schwierz, M. Croci-Maspoli, C. M. Grams, and H. Wernli, 2015: Importance of latent heat release in ascending air streams for atmospheric blocking. *Nat. Geosci.*, **8**, 610–614, doi: https://doi.org/10.1038/ngeo2487.

Rasmusson, E. M., and J. M. Wallace, 1983: Meteorological aspects of the El Niño/Southern Oscillation. *Science*, **222**, 1195–1202, doi: https://doi.org/10.1126/science.222.4629.1195.

Rasmusson, E. M., and K. Mo, 1993: Linkages between 200-mb tropical and extratropical circulation anomalies during the 1986–1989 ENSO cycle. *J. Climate*, **6**, 595–616, doi: https://doi.org/10.1175/1520-0442(1993)006<0595:LBMTAE>2.0.CO;2.

Rex, D. F., 1950: Blocking action in the middle troposphere and its effect upon regional climate. Part I: An aerological study of blocking action. *Tellus*, **2A**, 196–211, doi: https://doi.org/10.1111/j.2153-3490.1950.tb00331.x.

Riemer, M., S. C. Jones, and C. A. Davis, 2008: The impact of extratropical transition on the downstream flow: An idealized modelling study with a straight jet. *Quart. J. Roy. Meteor. Soc.*, **134**, 69–91, doi: https://doi.org/10.1002/qj.189.

Saha, S., and Coauthors, 2010: The NCEP Climate Forecast System Reanalysis. *Bull. Amer. Meteor. Soc.*, **91**, 1015–1058, doi: https://doi.org/10.1175/2010BAMS3001.1.

Saha, S., and Coauthors, 2014: The NCEP Climate Forecast System version 2. *J. Climate*, **27**, 2185–2208, doi: https://doi.org/10.1175/JCLI-D-12-00823.1.

Schubert, S. D., and C. Park, 1991: Low-frequency intraseasonal tropical–extratropical interactions. *J. Atmos. Sci.*, **48**, 629–650, doi: https://doi.org/10.1175/1520-0469(1991)048<0629:LFITEI>2.0.CO;2.

Sheng, J., 2002: GCM experiments on changes in atmospheric predictability associated with the PNA pattern and tropical SST anomalies. *Tellus*, **54A**, 317–239, doi: 10.1034/j.1600-0870.2002.01324.x.

Strong, C., and R. E. Davis, 2008: Variability in the position and strength of winter jet stream cores related to Northern Hemisphere teleconnections. *J. Climate*, **21**, 584–592, doi: https://doi.org/10.1175/2007JCLI1723.1.

Tibaldi, S., and F. Molteni, 1990: On the operational predictability of blocking. *Tellus*, **42A**, 343–563.

Thompson, D. W. J., and J. M. Wallace, 1998: The Arctic oscillation signature in wintertime geopotential height and temperature fields. *Geophys. Res. Lett.*, **25**, 1297–1300.

Torn, R. D., 2010: Diagnosis of the downstream ridging associated with extratropical transition using short-term ensemble forecasts. *J. Atmos. Sci.*, **67**, 817–833, doi: https://doi.org/10.1175/2009JAS3093.1.

Torn, R. D., and G. J. Hakim, 2015: Comparison of wave packets associated with extratropical transition and winter cyclones. *Mon. Wea. Rev.*, **143**, 1782–1803, doi: https://doi.org/10.1175/MWR-D-14-00006.1.

Wallace, J. M., and D. S. Gutzler, 1981: Teleconnections in the geopotential height field during the Northern Hemisphere winter. *Mon. Wea. Rev.*, **109**, 784–812.

Wang, L., and W. Chen, 2014: An intensity index for the East Asian winter monsoon. *J. Climate*, **27**, 2361–2374, doi: https://doi.org/10.1175/JCLI-D-13-00086.1.

Wilks, D. S., 2011: Statistical Methods in the Atmospheric Sciences. 3rd ed. Elsevier, 676 pp.

Xie, Z., Y. Du, and S. Yang, 2015: Zonal extension and retraction of the subtropical westerly jet stream and evolution of precipitation over East Asia and the western Pacific. *J. Climate*, **28**, 6783–6798, doi: https://doi.org/10.1175/JCLI-D-14-00649.1.

Yang, S., K. M. Lau, and K. M. Kim, 2002: Variations of the East Asian jet stream and Asian–Pacific–American winter climate anomalies. *J. Climate*, **15**, 306–325, doi: https://doi.org/10.1175/1520-0442(2002)015<0306:VOTEAJ>2.0.CO;2.

Table Captions

TABLE 1. Characteristic residence times in days for each NPJ regime. The numbers in parentheses represent the number of unique periods characterized by each NPJ regime during September–May 1979–2014.

TABLE 2. NPJ Phase Diagram characteristics derived from the CFSR for the periods characterized by the best and worst NPJ Phase Diagram medium-range forecasts. Asterisks indicate that values associated with the best and worst forecasts are statistically different at the 99.9% confidence level.

Tables

General NPJ Regime Characteristics				
NPJ Regime	Mean Residence Time (d)	Median Residence Time (d)	Maximum Residence Time (d)	Minimum Residence Time (d)
Jet Extension (N=380)	3.85	2.50	27.25	0.25
Jet Retraction (N=383)	3.70	2.75	34.00	0.25
Poleward Shift (N=431)	3.58	2.75	18.00	0.25
Equatorward Shift (N=373)	3.65	2.50	18.50	0.25
Origin (N=872)	4.65	3.25	35.50	0.25

TABLE 1. Characteristic residence times in days for each NPJ regime. The numbers in parentheses represent the number of unique periods characterized by each NPJ regime during September–May 1979–2014.

Comparison of Best/Worst Forecast Periods					
	Avg. Start PC1	Avg. Start PC2	Avg. ΔPC1	Avg. ΔPC2	Avg. 10-d Traj. Length
Best Forecasts (N=475)	0.09*	0.04	0.09	0.16*	3.50*
Worst Forecasts (N=763)	–0.18*	–0.08	0.01	–0.21*	4.33*

TABLE 2. NPJ Phase Diagram characteristics derived from the CFSR for the periods characterized by the best and worst NPJ Phase Diagram medium-range forecasts. Asterisks indicate that values associated with the best and worst forecasts are statistically different at the 99.9% confidence level.

Figure Captions

FIG. 1. (a) September–May 250-hPa mean zonal wind contoured in black every 10 m s^{-1} above 30 m s^{-1} and the regression of the EOF1 onto 250-hPa zonal wind anomaly data is shaded following the legend in m s^{-1}. (b) As in (a) but for EOF2.

FIG. 2. (a) 250-hPa wind speed in m s^{-1} is shaded following the legend at 1800 UTC 11 February 2004. (b) The location of weighted PC1 and PC2 at 1800 UTC 11 February 2004 within the NPJ Phase Diagram. (c,d) As in (a,b) but for 1800 UTC 13 March 2009.

FIG. 3. Similar conventions as in Fig. 2 but for (a,b) 1800 UTC 9 April 1984 and (c,d) 1200 UTC 28 January 1991.

FIG. 4. Schematic illustrating the classification scheme for NPJ Phase Diagram forecasts.

FIG. 5. Composite mean 250-hPa wind speed in m s^{-1} is shaded in the fill pattern, 250-hPa geopotential height is contoured in black every 120 m, and 250-hPa geopotential height anomalies are contoured in solid red and dashed blue every 30 m for positive and negative values, respectively, 4 days following the initialization of a (a) jet extension, (b) jet retraction, (c) poleward shift, and (d) equatorward shift regime. Stippled areas represent locations where the 250-hPa geopotential height anomalies are statistically different from climatology at the 99% confidence interval.

FIG. 6. Composite anomalies of mean sea-level pressure are contoured in the solid and dashed black contours every 2 hPa for positive and negative values, respectively, and 850-hPa temperature anomalies are shaded in the fill pattern every 1 K 4 days following the initialization of a (a) jet extension, (b) jet retraction, (c) poleward shift, and (d) equatorward shift regime. Stippled areas represent locations where the 850-hPa temperature anomalies are statistically different from climatology at the 99% confidence interval.

FIG. 7. (a) The percent frequency of each NPJ regime during every cool season between 1979–2014. (b) The percent frequency of analysis times during each month of the cool season that are characterized by each NPJ regime. The numbers in parentheses below each month indicate the number of valid analysis times during each month.

FIG. 8. (a) The percent frequency of each NPJ regime at analysis times during which the NPJ is outside of the unit circle on the NPJ Phase Diagram and characterized by a PNA index > 0.5. The numbers in parentheses below each category indicate the number of valid analysis times in each category. (b) As in (a) but for the daily AO index. (c) As in (a) but for the monthly Nino3.4 index

FIG. 9. (a) The average error of GEFS ensemble mean NPJ Phase Diagram forecasts initialized during the same season. The colored circles on each line indicate that the error assocated with that regime is statistically different from the error associated with another season at the 99% confidence interval. (b) As in (a) but for forecasts initialized during the same NPJ regime. (c) As in (a) but for forecasts verifying during the same NPJ regime.

FIG. 10. The percent frequency that an NPJ regime is over forecast or under forecast by the GEFS ensemble mean NPJ Phase Diagram forecasts relative to the verifying 0-h analysis at each forecast lead time.

FIG. 11. Schematic illustrating the classification scheme for the best and worst NPJ Phase Diagram medium-range forecasts.

FIG. 12. (a) The percent frequency of the best and worst NPJ Phase Diagram medium-range forecasts that are initialized during each month of the cool season. (b) The percent frequency of the best and worst NPJ Phase Diagram medium-range forecasts that are initialized during each NPJ regime.

FIG. 13. Composite mean 250-hPa wind speed in m s^{-1} is shaded in the fill pattern, 250-hPa geopotential height is contoured in black every 120 m, and 250-hPa geopotential height anomalies are contoured in the red and dashed blue contours every 30 m for positive and negative values, respectively, at the time a (a) best and (b) worst NPJ Phase Diagram forecast is initialized during a jet extension. (c,d) As in (a,b) but for those forecasts initialized during a jet retraction. (e,f) As in (a,b) but for those forecasts initialized during a poleward shift. (g,h) As in (a,b) but for those forecasts initialized during an equatorward shift.

FIG. 14. (a) The difference between the 250-hPa geopotential height anomalies associated with a worst and best NPJ Phase Diagram forecast at the time of forecast initialization during a jet

extension is shaded every 30 m in the fill pattern. (b) As in (a) but for a jet retraction. (c) As in (a) but for a poleward shift. (d) As in (a) but for an equatorward shift. Statistically significant differences in geopotential height anomalies at the 99% confidence interval are stippled in all panels.

FIG. 15. Similar conventions as in Fig. 13, but for the composite 250-hPa flow pattern 192 h following the initialization of a best and worst NPJ Phase Diagram forecast.

FIG. 16. Similar conventions as in Fig. 14, but for the composite difference between 250-hPa geopotential height anomalies associated with the upper-tropospheric flow pattern 192 h following the initialization of a worst and best NPJ Phase Diagram forecast.

Figures

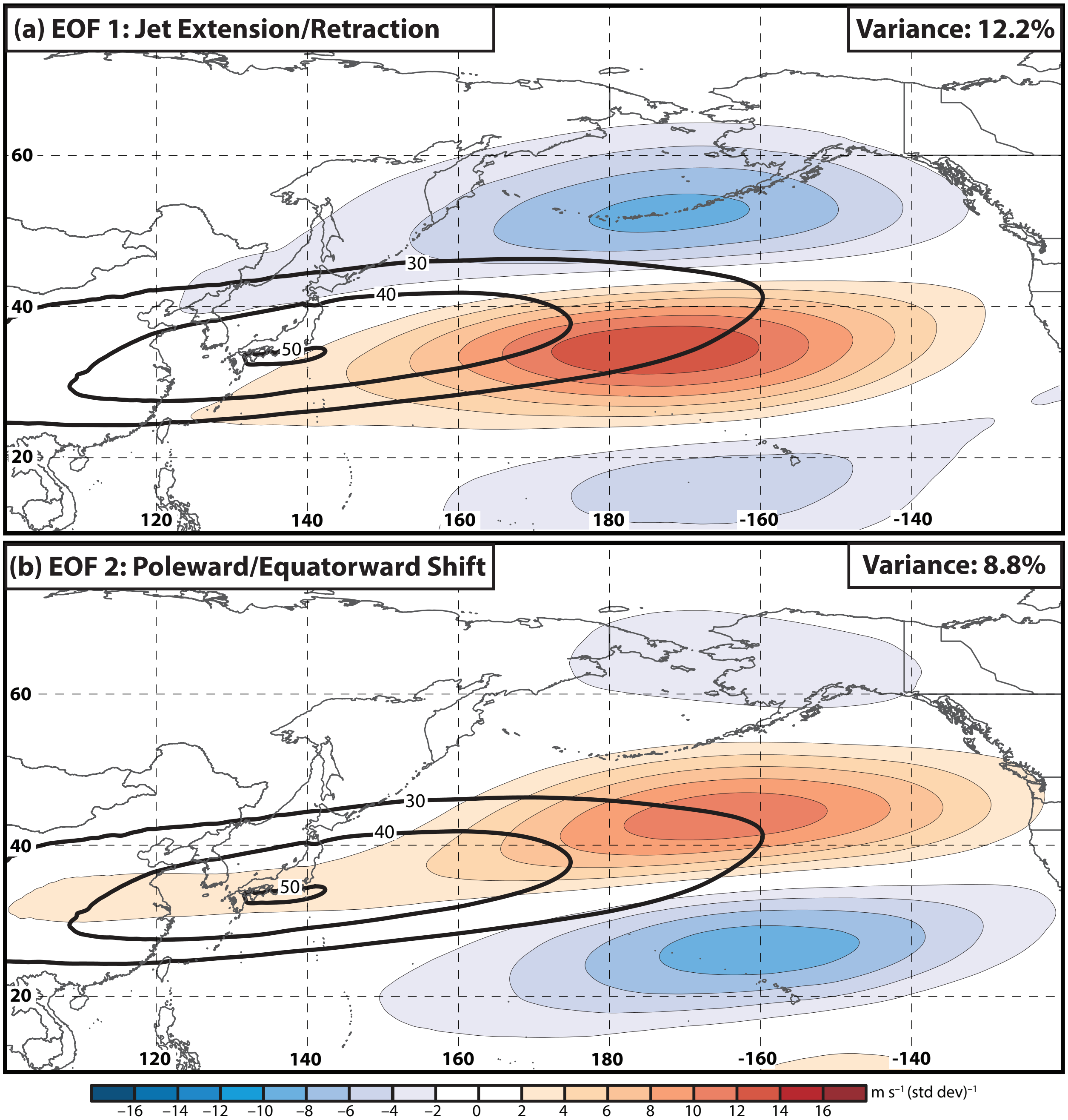

FIG. 1. (a) September–May 250-hPa mean zonal wind contoured in black every 10 m s^{-1} above 30 m s^{-1} and the regression of the EOF1 onto 250-hPa zonal wind anomaly data is shaded following the legend in m s^{-1}. (b) As in (a) but for EOF2.

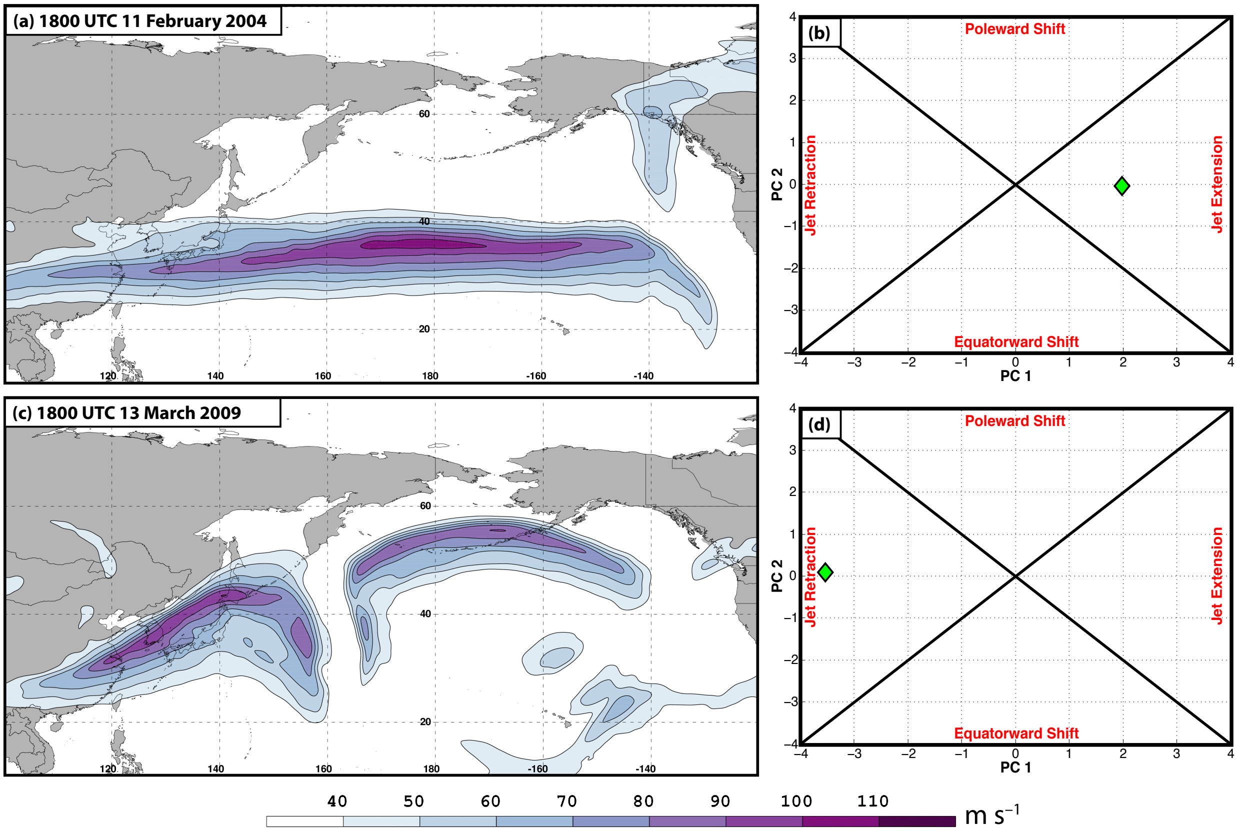

FIG. 2. (a) 250-hPa wind speed in m s^{-1} is shaded following the legend at 1800 UTC 11 February 2004. (b) The location of weighted PC 1 and PC 2 at 1800 UTC 11 February 2004 within the NPJ Phase Diagram. (c,d) As in (a,b) but for 1800 UTC 13 March 2009.

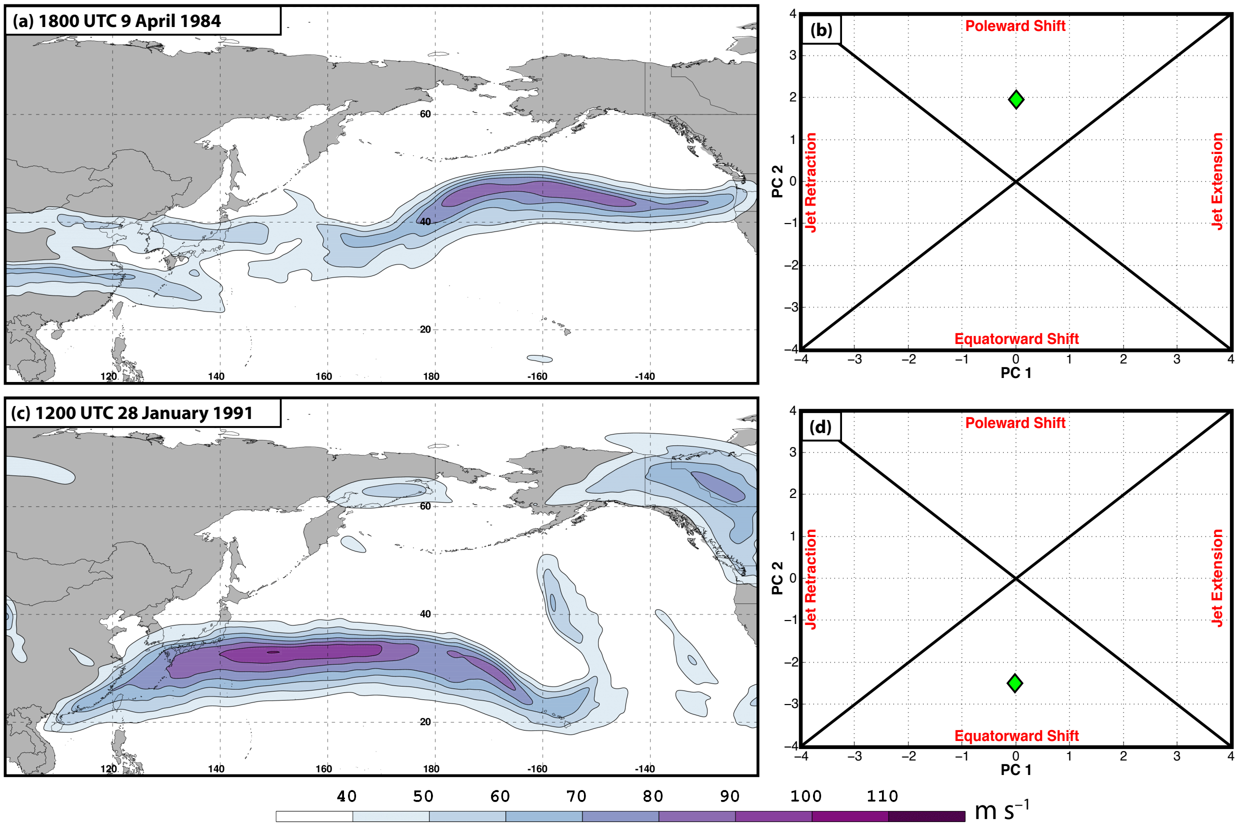

FIG. 3. Similar conventions as in Fig. 2 but for (a,b) 1800 UTC 9 April 1984 and (c,d) 1200 UTC 28 January 1991.

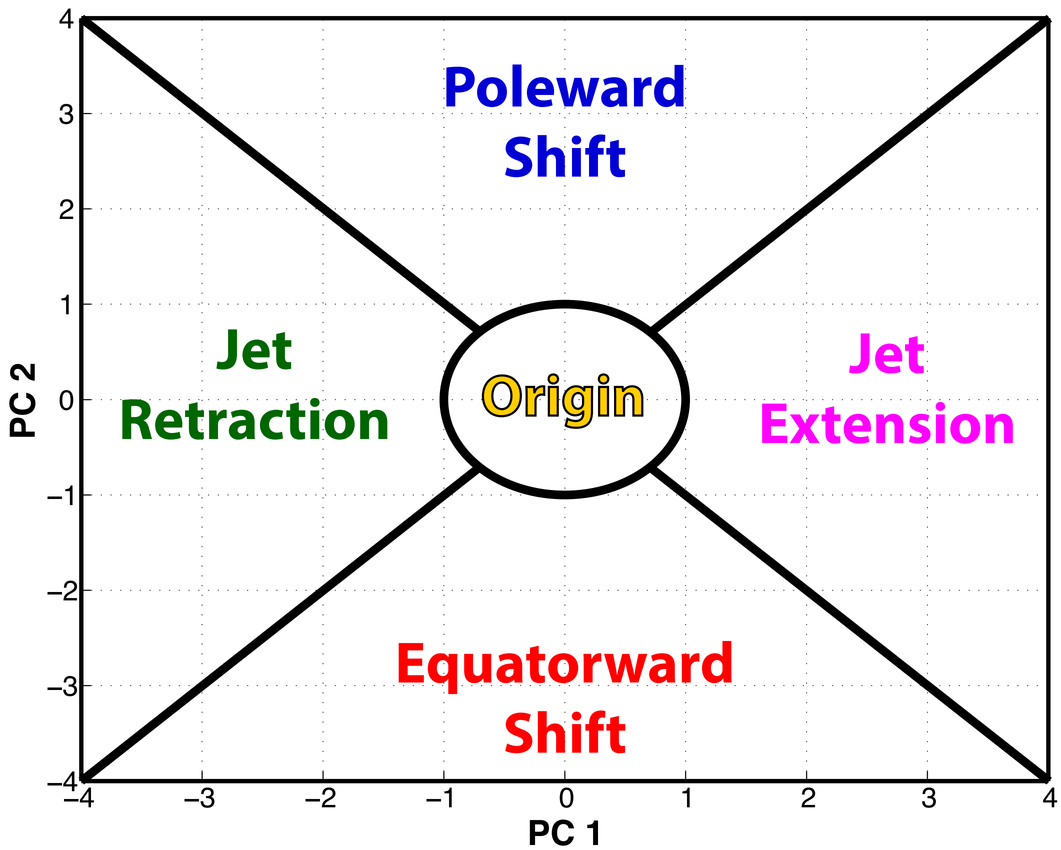

FIG. 4. Schematic illustrating the classification scheme for NPJ Phase Diagram forecasts.

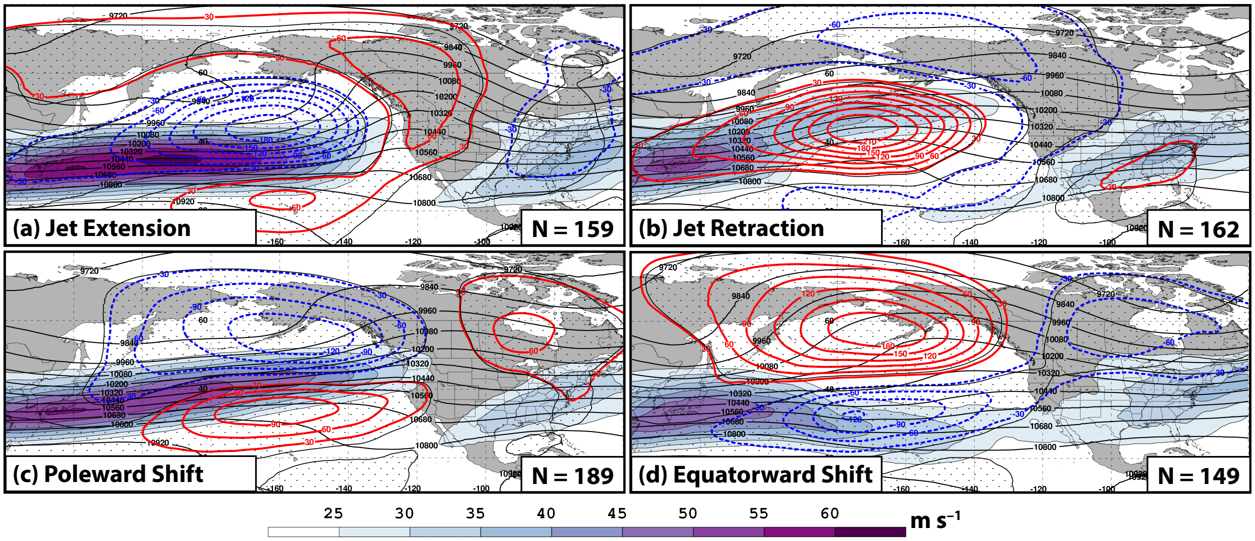

FIG. 5. Composite mean 250-hPa wind speed in m s^{-1} is shaded in the fill pattern, 250-hPa geopotential height is contoured in black every 120 m, and 250-hPa geopotential height anomalies are contoured in solid red and dashed blue every 30 m for positive and negative values, respectively, 4 days following the initialization of a (a) jet extension, (b) jet retraction, (c) poleward shift, and (d) equatorward shift regime. Stippled areas represent locations where the 250-hPa geopotential height anomalies are statistically different from climatology at the 99% confidence interval.

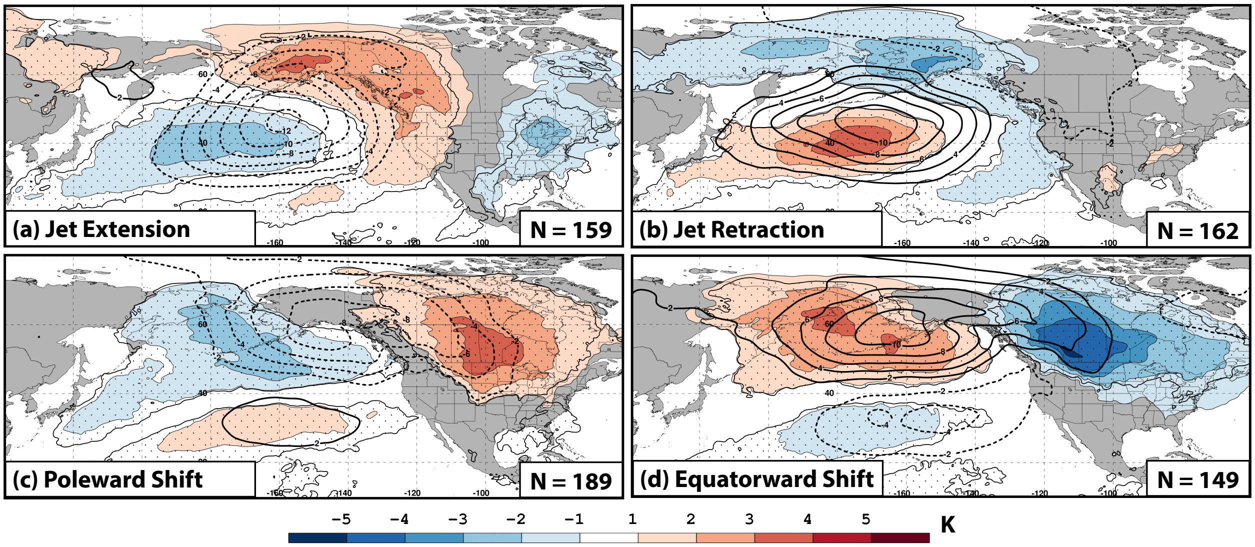

FIG. 6. Composite anomalies of mean sea-level pressure are contoured in the solid and dashed black contours every 2 hPa for positive and negative values, respectively, and 850-hPa temperature anomalies are shaded in the fill pattern every 1 K 4 days following the initialization of a (a) jet extension, (b) jet retraction, (c) poleward shift, and (d) equatorward shift regime. Stippled areas represent locations where the 850-hPa temperature anomalies are statistically different from climatology at the 99% confidence interval.

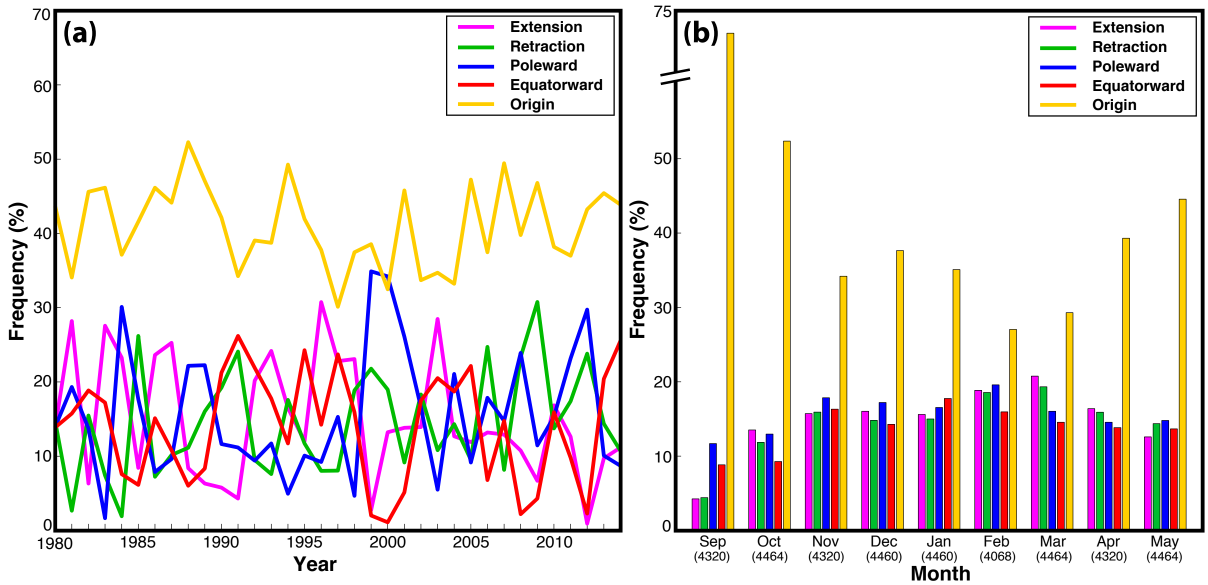

FIG. 7. (a) The percent frequency of each NPJ regime during every cool season between 1979–2014. (b) The percent frequency of analysis times during each month of the cool season that are characterized by each NPJ regime. The numbers in parentheses below each month indicate the number of valid analysis times during each month.

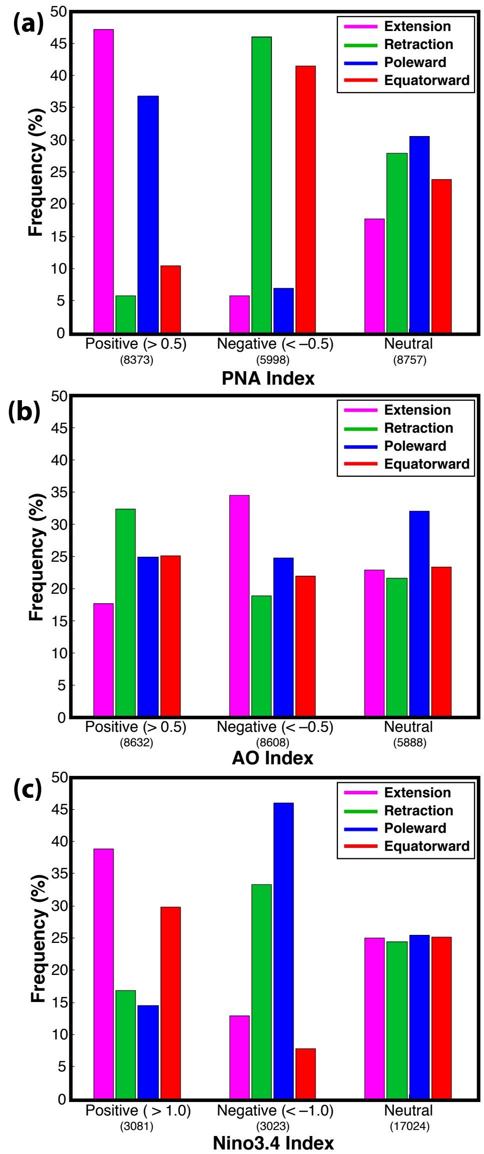

FIG. 8. (a) The percent frequency of each NPJ regime at analysis times during which the NPJ is outside of the unit circle on the NPJ Phase Diagram and characterized by a PNA index > 0.5. The numbers in parentheses below each category indicate the number of valid analysis times in each category. (b) As in (a) but for the daily AO index. (c) As in (a) but for the monthly Nino3.4 index

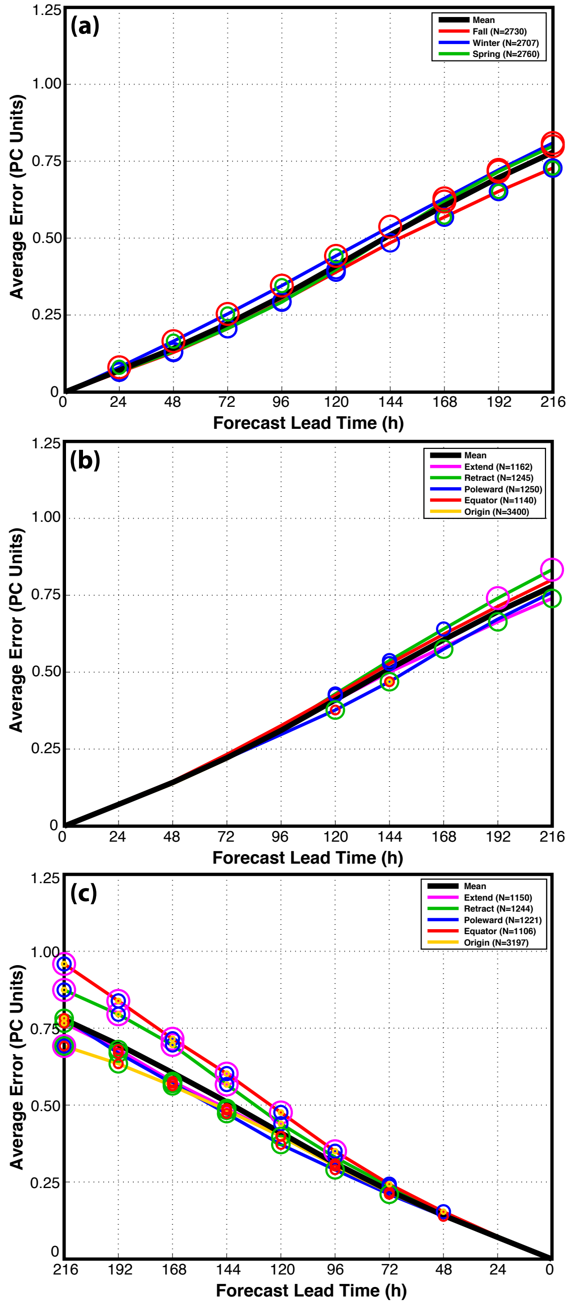

FIG. 9. (a) The average error of GEFS ensemble mean NPJ Phase Diagram forecasts initialized during the same season. The colored circles on each line indicate that the error assocated with that regime is statistically different from the error associated with another season at the 99% confidence interval. (b) As in (a) but for forecasts initialized during the same NPJ regime. (c) As in (a) but for forecasts verifying during the same NPJ regime.

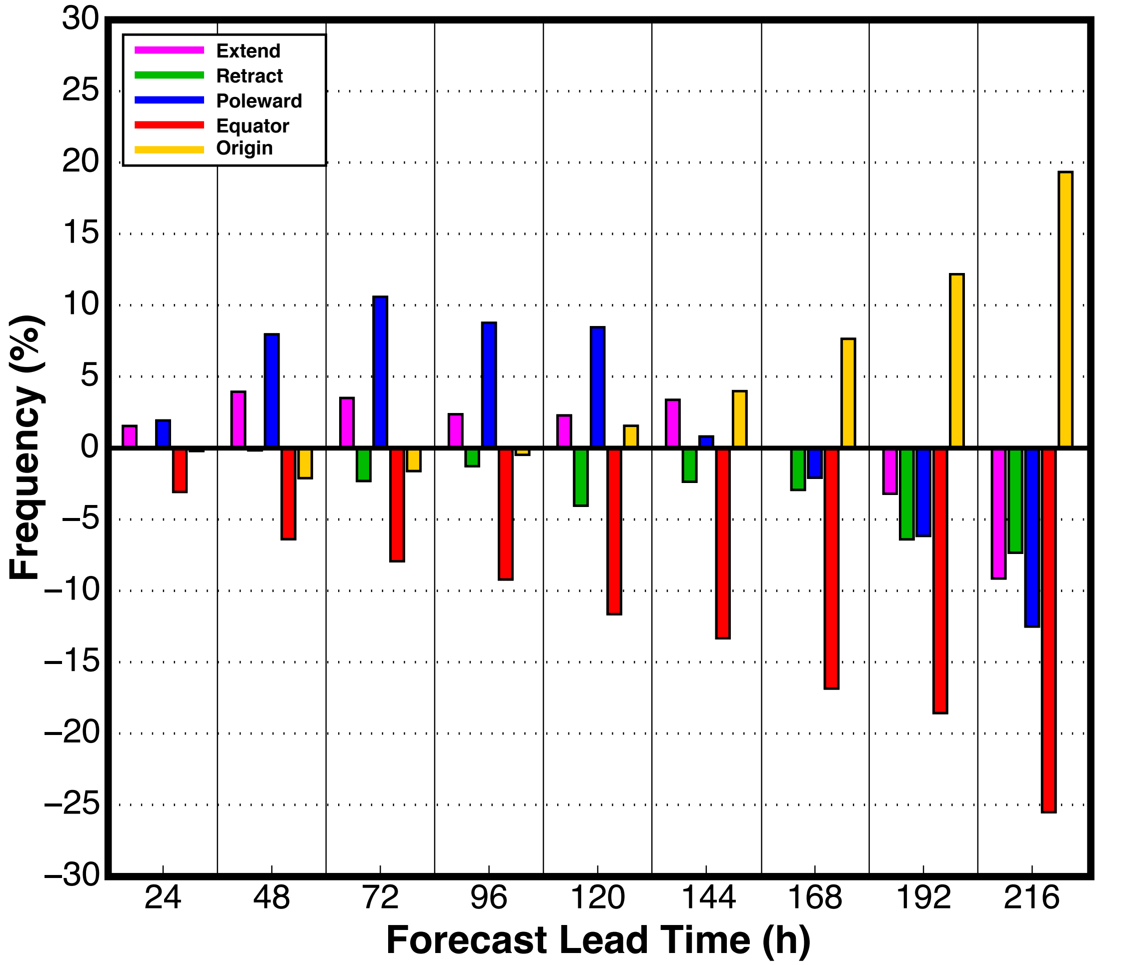

FIG. 10. The percent frequency that an NPJ regime is over forecast or under forecast by the GEFS ensemble mean NPJ Phase Diagram forecasts relative to the verifying 0-h analysis at each forecast lead time.

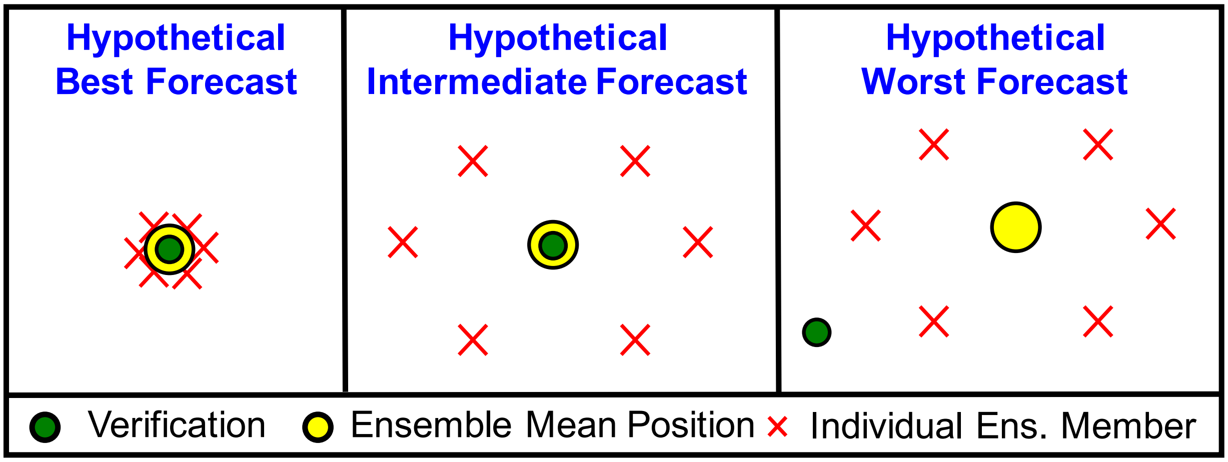

FIG. 11. Schematic illustrating the classification scheme for the best and worst NPJ Phase Diagram medium-range forecasts.

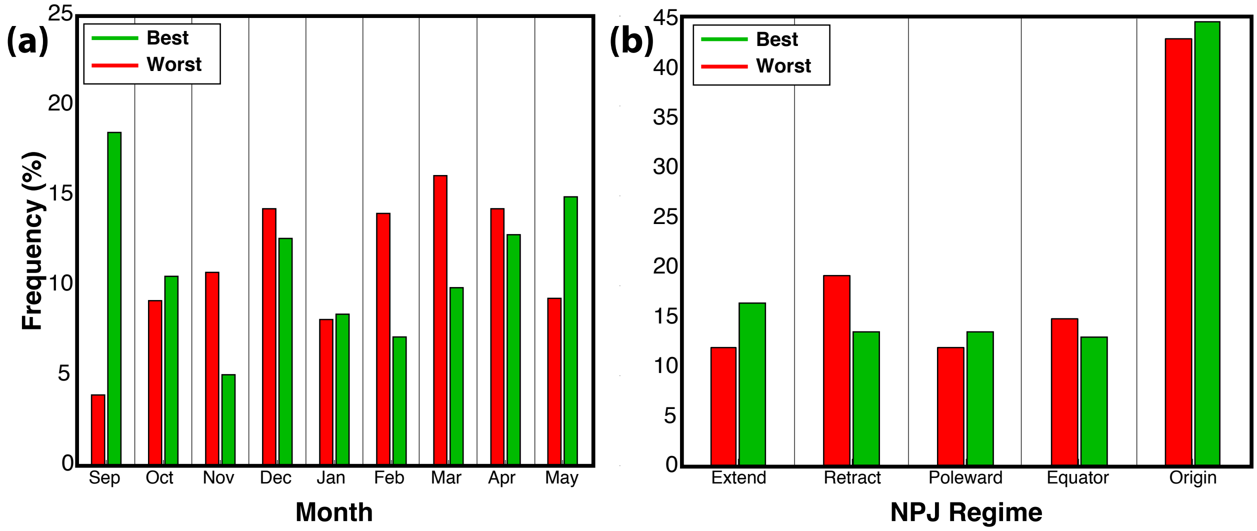

FIG. 12. (a) The percent frequency of the best and worst NPJ Phase Diagram medium-range forecasts that are initialized during each month of the cool season. (b) The percent frequency of the best and worst NPJ Phase Diagram medium-range forecasts that are initialized during each NPJ regime.

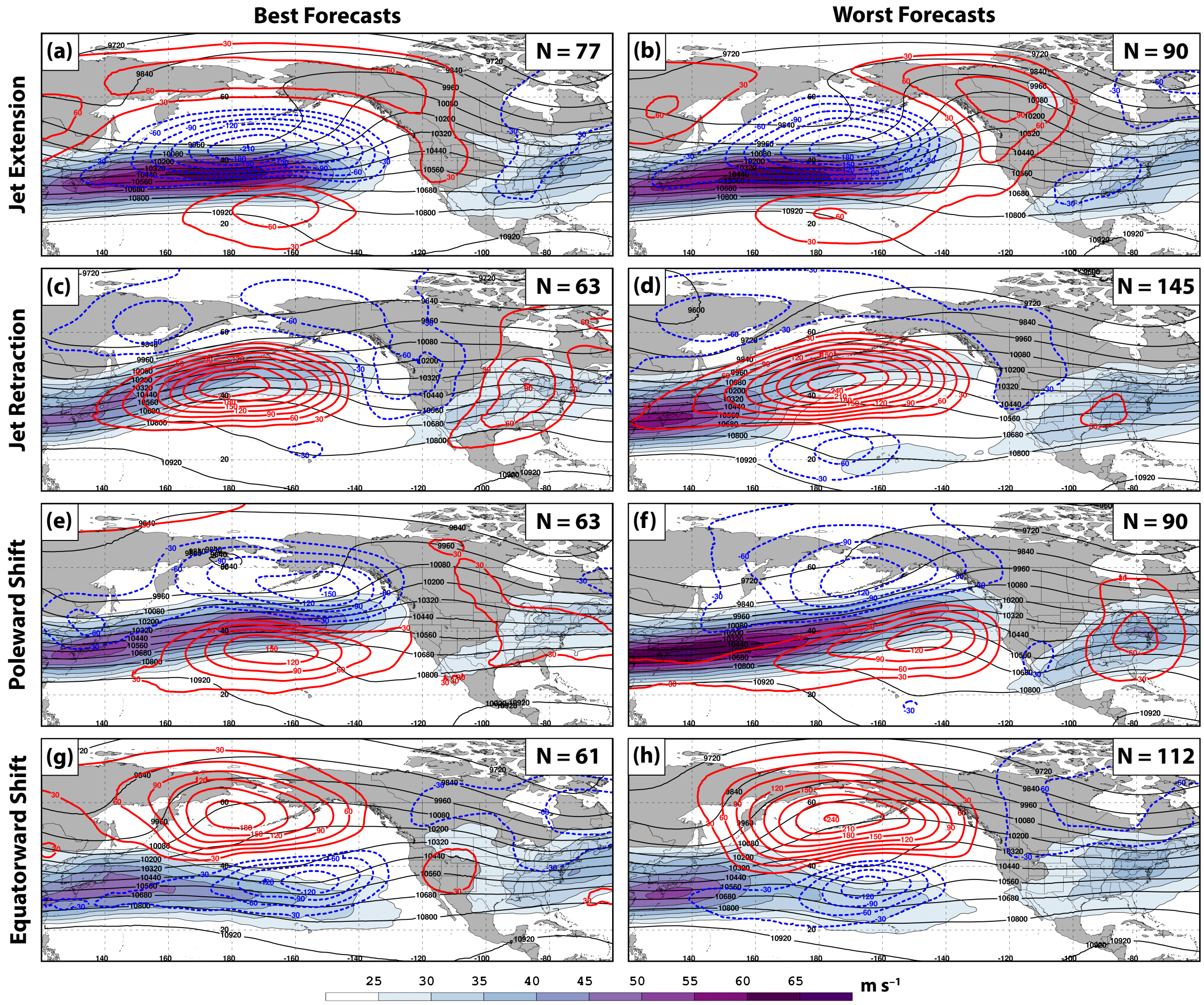

FIG. 13. Composite mean 250-hPa wind speed in m s^{-1} is shaded in the fill pattern, 250-hPa geopotential height is contoured in black every 120 m, and 250-hPa geopotential height anomalies are contoured in the red and dashed blue contours every 30 m for positive and negative values, respectively, at the time a (a) best and (b) worst NPJ Phase Diagram forecast is initialized during a jet extension. (c,d) As in (a,b) but for those forecasts initialized during a jet retraction. (e,f) As in (a,b) but for those forecasts initialized during a poleward shift. (g,h) As in (a,b) but for those forecasts initialized during an equatorward shift.

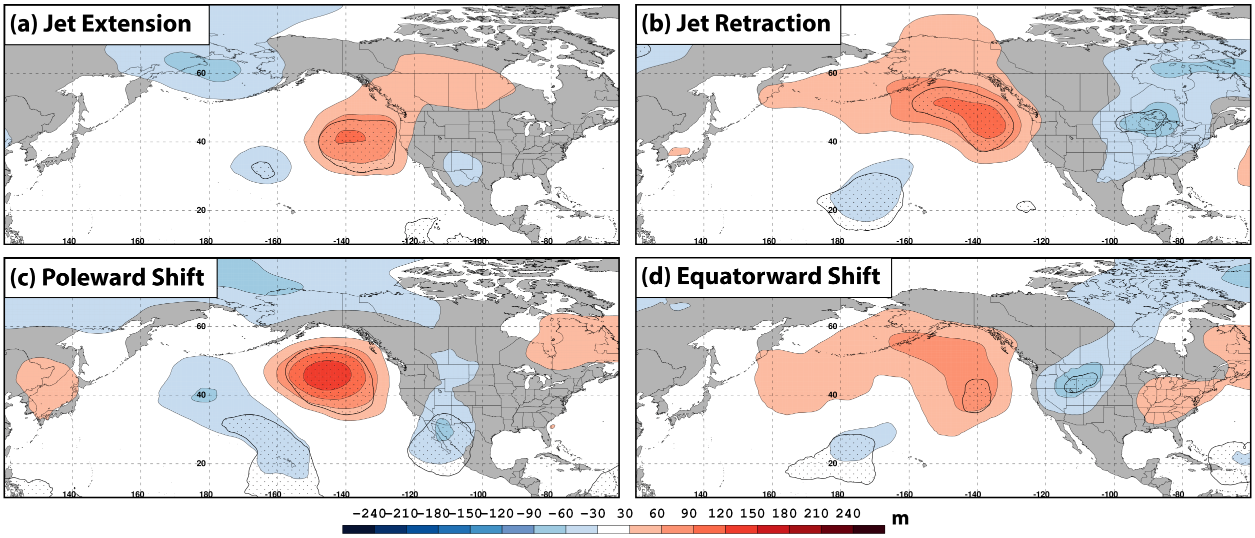

FIG. 14. (a) The difference between the 250-hPa geopotential height anomalies associated with a worst and best NPJ Phase Diagram forecast at the time of forecast initialization during a jet extension is shaded every 30 m in the fill pattern. (b) As in (a) but for a jet retraction. (c) As in (a) but for a poleward shift. (d) As in (a) but for an equatorward shift. Statistically significant differences in geopotential height anomalies at the 99% confidence interval are stippled in all panels.

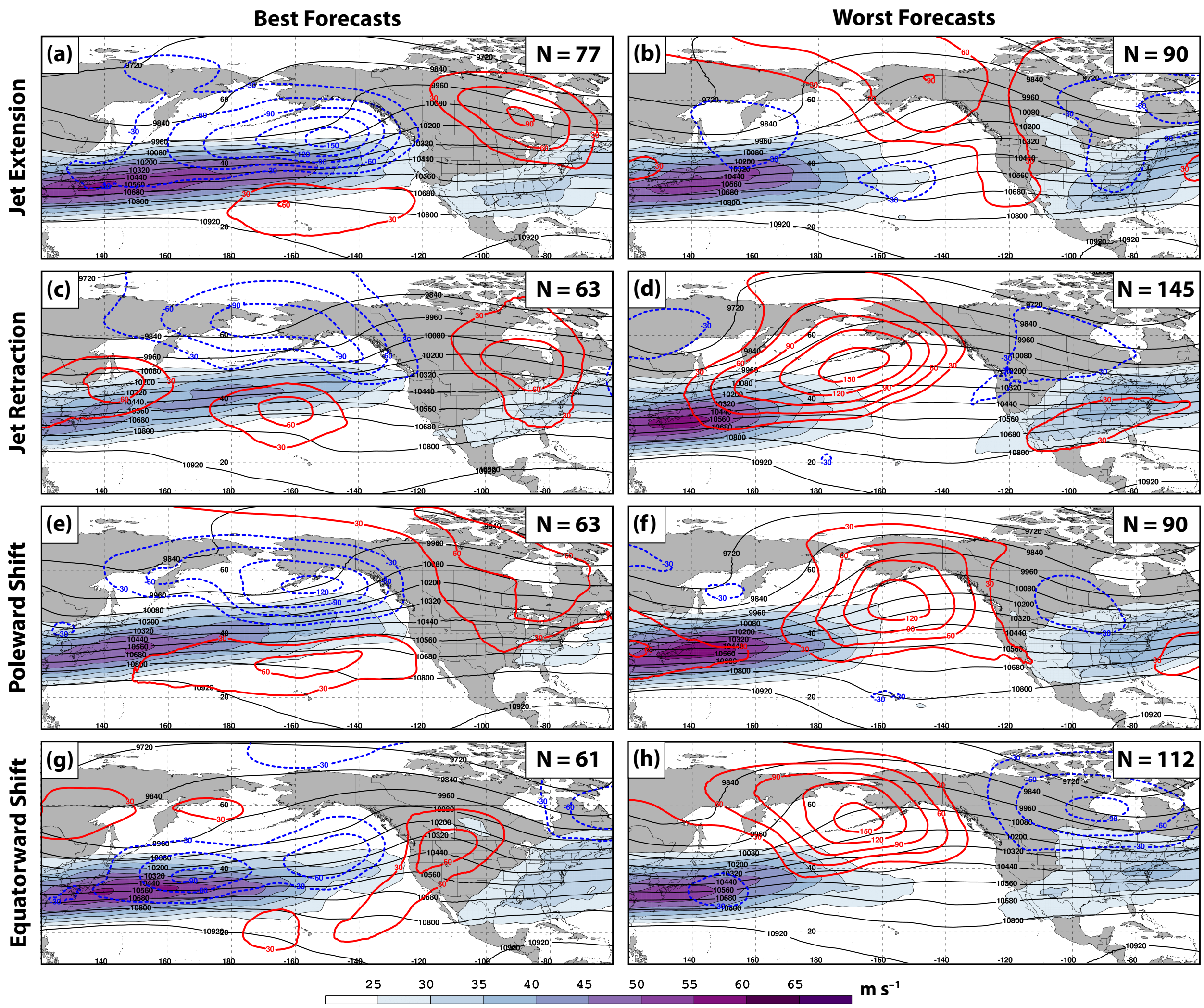

FIG. 15. Similar conventions as in Fig. 13, but for the composite 250-hPa flow pattern 192 h following the initialization of a best and worst NPJ Phase Diagram forecast.

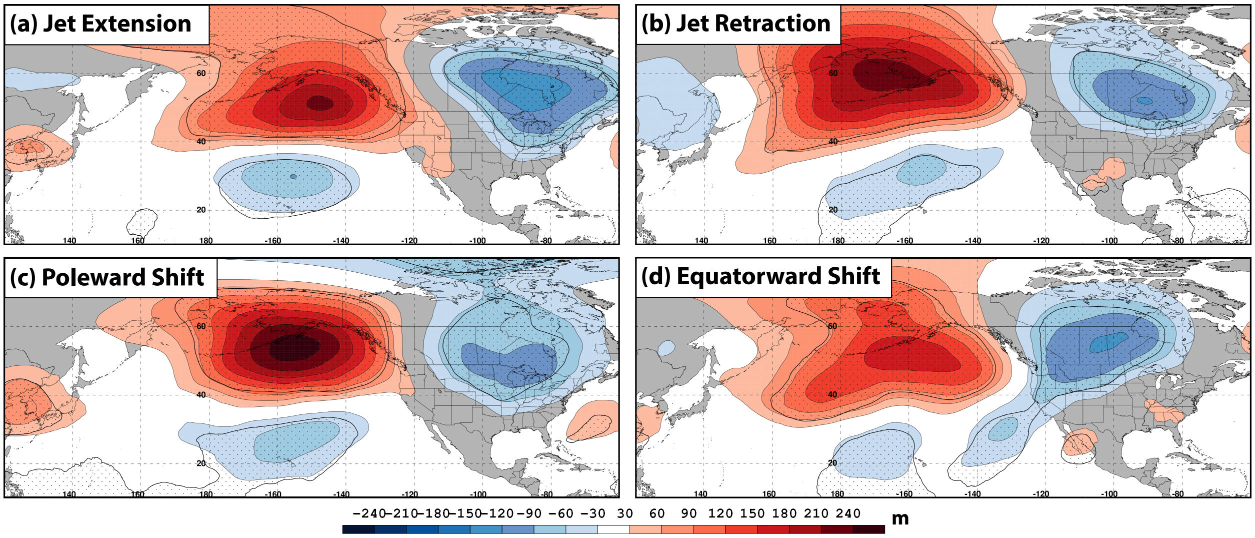

FIG. 16. Similar conventions as in Fig. 14, but for the composite difference between 250-hPa geopotential height anomalies associated with the upper-tropospheric flow pattern 192 h following the initialization of a worst and best NPJ Phase Diagram forecast.